JOURNAL OF GEOPHYSICAL RESEARCH, VOL. 114, B09406, doi:10.1029/2008JB005935, 2009

Polyphase formation and exhumation of high- to ultrahigh-pressure rocks in continental subduction zone: Numerical modeling and application to the Sulu ultrahigh-pressure terrane in eastern China

Zhonghai Li[1,2] and Taras V. Gerya[2,3]

Received 16 July 2008; revised 23 May 2009; accepted 30 June 2009; published 22 September 2009.

[1] High- to ultrahigh-pressure (HP-UHP) metamorphic rocks commonly form and exhume during the early continental collision, and many questions related to their origin still remain unresolved. We focus our study on explaining the poly metamorphic origins of many HP-UHP terranes composed of tectonic units having strongly variable ages, peak metamorphic conditions, and P-T paths. These features are especially well characterized for the Sulu UHP terrane in eastern China which we have chosen therefore as the reference case. We conducted 2-D thermomechanical numerical modeling of continental subduction associated with formation and exhumation of HP-UHP rocks. Our experiments suggest existence of several consequent episodes of (U)HP rocks exhumation related to the inherently cyclic origin of continental crust subduction-detachment-exhumation processes. Three major phases of these processes are identified in our reference model for the Sulu UHP terrane: (1) first and (2) second exhumation episodes of HP rocks originated in the subduction channel at lithospheric depths and (3) exhumation of UHP rocks originated at asthenospheric depths. Numerical models also suggest that subducted UHP rocks which are positively buoyant compared to the mantle may detach from the slab forming a flattened plume underplating the overriding lithosphere. This sublithospheric plume may exist for several million years being heated to 800–900°C by the surrounding hot mantle. At the later stage, upward extrusion of hot partially molten rocks from the plume may exhume high-temperature (HT) UHP complexes toward the surface.

Citation: Li, Z., and T. V. Gerya (2009), Polyphase formation and exhumation of high- to ultrahigh-pressure rocks in continental subduction zone: Numerical modeling and application to the Sulu ultrahigh-pressure terrane in eastern China, *J. Geophys. Res.*, *114*, B09406, doi:10.1029/2008JB005935.

1. Introduction

[2] Occurrences of ultrahigh-pressure (UHP) terranes around the world have been increasingly recognized with more than 20 UHP terranes documented [e.g., *Liou et al.*, 2004]. It has been suggested that the HP-UHP metamorphism can be considered as a ''hallmark'' for the modern plate tectonics regime characterized by ''colder'' subduction and started from a Neoproterozoic time [e.g., *Brown*, 2006, 2007]. Growing evidences are being discovered in the Phanerozoic collision belts of the burial of crustal rocks to depths on the order of 150–200 km and of subsequent exhumation from such depths [e.g., *Chopin*, 2003] within the time scale of shortly before or during the early continental collision [e.g., *Liou et al.*, 2004].

[3] Besides the systematic geological/petrological studies of the UHP terranes, analog [e.g., *Chemenda et al.*, 1995, 1996, 2000; *Boutelier et al.*, 2004] and numerical modeling [e.g., *Beaumont et al.*, 2001; *Burov et al.*, 2001; *Toussaint et al.*, 2004a; *Burg and Gerya*, 2005; *Gerya et al.*, 2008; *Yamato et al.*, 2007, 2008; *Warren et al.*, 2008a, 2008b; *Currie et al.*, 2007] become more and more important for investigating the continental subduction processes associated with burial and exhumation of crustal rocks. Two contrasting tectonic styles of continental subduction are predicted on the basis of numerical experiments: one-sided subduction (overriding plate does not subduct) and two-sided subduction (both plates subduct together) [*Tao and O'Connell*, 1992; *Pope and Willett*, 1998; *Faccenda et al.*, 2008; *Warren et al.*, 2008a], also with some other intermediate possibilities; while only the one-sided subduction can produce significant syntectonic UHP rocks exhumation [*Warren et al.*, 2008a]. On the basis of the analog and numerical modeling studies, processes of HP-UHP rocks exhumation can be divided into the following groups: (1) syncollisional exhumation of coherent and buoyant crustal slab, with weak zone formation at the entrance zone

[1]Department of Earth Sciences, Nanjing University, Nanjing, China.
[2]Geophysical Fluid Dynamics, Institute of Geophysics, Department of Earth Sciences, ETH-Zurich, Zurich, Switzerland.
[3]Also at Geology Department, Moscow State University, Moscow, Russia.

0148-0227/09/2008JB005935$09.00

of subduction channel [*Chemenda et al.*, 1995, 1996; *Toussaint et al.*, 2004a], that can be accompanied by delamination of the subducting lithosphere [*Boutelier et al.*, 2004]; (2) episodic ductile extrusion of HP-UHP rocks from the subduction channel to the surface or crustal depths [*Beaumont et al.*, 2001; *Warren et al.*, 2008a]; and (3) continuous material circulation in the rheologically weak subduction channel stabilized at the plate interface, with materials exhumed from different depths [*Burov et al.*, 2001; *Gerya et al.*, 2002; *Stöckhert and Gerya*, 2005; *Yamato et al.*, 2007; *Warren et al.*, 2008a].

[4] Despite the significant recent progresses in modeling of HP-UHP metamorphic rocks formation and exhumation, some constraints from natural UHP terranes are still difficult to reconcile numerically:

[5] First, in numerical models the HP and UHP rocks in the subduction channel usually start to exhume nearly at the same time (<5 Ma) [e.g., *Warren et al.*, 2008a; *Yamato et al.*, 2008]. So the temporal discrepancies between HP-UHP slices are not notable. In contrast, the metamorphic ages of different slices in the same natural HP-UHP terrane are often discrepant (>10 Ma), e.g., the Sulu UHP terrane in eastern China (reviewed by *Xu et al.* [2006a]), which strongly indicates poly phase origin of HP-UHP metamorphism and exhumation processes.

[6] Second, high- to ultrahigh-pressure conditions are easily achieved in majority of models. In contrast the maximal peak temperature conditions of HP-UHP rocks in numerical experiments are usually $\geq$ 100°C lower than those extracted from natural data [e.g., *Stöckhert and Gerya*, 2005; *Yamato et al.*, 2007, 2008; *Warren et al.*, 2008a] with usual explanations related to uncertainties in heat generations within the lithosphere.

[7] Third, for the recognized UHP terranes, the exhumed HP-UHP units are usually present in the upper continental crust as thin, subhorizontal slabs bounded by faults or ductile shear zones and regional HP-UHP metamorphic zoning pattern is recognized in cases [e.g., *Frey et al.*, 1999; *Carswell et al.*, 1999; *Kaneko et al.*, 2000; *Liou et al.*, 2004; *Xu et al.*, 2006a]. However, direct structural metamorphic comparison between numerical models and natural UHP terranes is often precluded by insufficient spatial resolution of conducted numerical experiments.

[8] In this paper we aim to address these issues by conducting 2-D thermomechanical numerical experiments allowing for investigating the burial and exhumation processes of HP-UHP metamorphic rocks. We also discuss the comparison of our numerical results with the reference case of Sulu UHP terrane in eastern China, one of the largest and best preserved UHP belt around the world with detailed geological, petrological and geophysical constraints being available [e.g., *Ernst and Liou*, 1995; *Hacker et al.*, 2000; *Faure et al.*, 2003; *Zheng et al.*, 2003; *D. Liu et al.*, 2006; *Xu et al.*, 2006a, 2006b].

2. Geological Setting of the Sulu UHP Terrane

[9] The Qinling-Dabie-Sulu orogenic belt in central China was created by Triassic collision between the North China and Yangtze cratons (Figure 1a, inset). It extends ~2000 km from the western Qinling Mountains through Tongbai to the Dabie Mountains. As the eastern extension of this orogenic belt, the Sulu terrane has been displaced northward ~500 km by the Tan-Lu fault [e.g., *Liou et al.*, 1995; *Wang et al.*, 1995; *Zhang et al.*, 2003]. The Sulu HP-UHP metamorphic terrane extends NE-SW for ~750 km and is 180 km wide. It is bounded on the north by the Wulian-Yantai fault (WYF) and the Laiyang Cretaceous basin, on the south by the Jiashan-Xiangshui fault (JXF) and the north Jiangsu basin, and on the west by the Tan-Lu fault (Figure 1a) [*Xu et al.*, 2006a]. According to field observations, the Sulu terrane consists of tectonic slices (HP-UHP metamorphic rocks) bounded by ductile shear zones (Figures 1a and 1b) with the following geological/petrological characteristics.

2.1. Spatial Distribution of Metamorphic Units

[10] From the north to south, the Sulu terrane is composed of slices with decreasing metamorphic pressure from UHP (3 and 4, ultrahigh pressure, Figure 1) to VHP (2, very high pressure, Figure 1), and HP (1, high pressure, Figure 1). According to the rock types, the UHP slices can be subdivided into two sections: granitic gneisses dominated (4, protolith mainly of granitic rocks) and paragneiss dominated (3, protolith mainly of sediment).

2.2. Temporal Constraints

[11] Radiometric data from numerous U/Pb, Sm/Nd, Rb/Sr, Ar/Ar studies suggest that metamorphism and exhumation of UHP rocks in the Sulu area occurred in 240–220 Ma and 220–200 Ma, respectively, while the HP slices (limited data) formed before 250 Ma and were exhumed from 250 to 210 Ma [*D. Liu et al.*, 2006; *Xu et al.*, 2006a]. Therefore, the metamorphism and exhumation of the HP slices are more than 10 Ma earlier than the UHP slices, which indicates the polyphase/differential subduction and exhumation processes of the HP and UHP rocks.

2.3. Rock Types and Protoliths

[12] According to the field observations and borehole samples, lithologies of the Sulu terrane can be subdivided into five groups [*Zhang et al.*, 2000; *Liu et al.*, 2004; *Zhang et al.*, 2006]: ultramafic rocks (e.g., peridotite), mafic rocks (e.g., eclogite), intermediate felsic rocks (e.g., gneiss and schist), silicate rocks (e.g., quartzite) and carbonate rocks (e.g., marble). The paragneiss, granitic gneiss, marble and quartzite that host the eclogite and ultramafic boudins and lenses account for ~95 vol % of the Sulu terrane [*Xu et al.*, 2006a]. The protoliths of the Sulu UHP terrane are mainly the Yangtze continental crust that was subducted to a depth >100 km and then exhumed rapidly [e.g., *Cong and Wang*, 1999].

2.4. P-T Conditions

[13] Metamorphic P-T conditions (paths) are among the most important constraints for subduction and exhumation as well as many other tectonic processes that can produce P-T records in the metamorphic rocks [e.g., *Wakabayashi*, 2004]. For the Sulu UHP terrane, detailed petrological studies revealed the following P-T conditions of different metamorphic slices (Figures 1a and 1b): HP 1, early blueschist facies metamorphism at 0.7–0.85 GPa and 300–360°C followed by greenschist retrogression at 0.2–0.4 GPa and 350–410°C [*Qiu and Xu*, 2002]; VHP 2, peak metamorphic

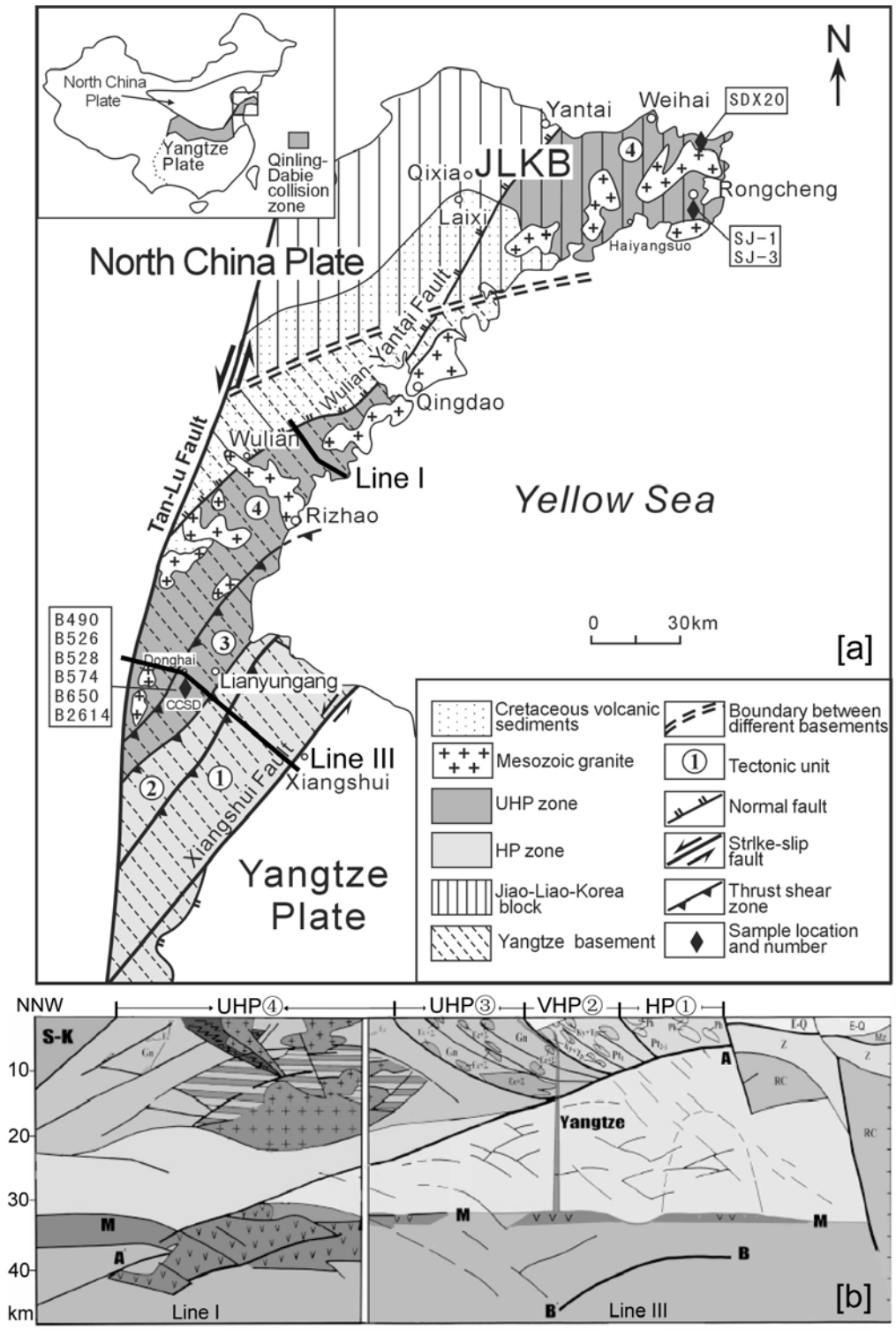

Figure 1. Geological setting of Sulu UHP terrane in eastern China. (a) Tectonic sketch map of Sulu HP-UHP metamorphic terrane [*Xu et al.*, 2006a] showing high-pressure zone 1, very high pressure (VHP) zone 2, and UHP (3 and 4) zones separated by ductile shear zones. CCSD, location of the Chinese Continental Scientific Drilling project site. The latitude and longitude scales of this map are 33–38°N and 118–123°E, respectively. (b) The inferred crustal structures of the integrated profiles along the line I and line III in Figure 1a [*Yang*, 2002]. S-K, Sino-Korean craton (or north China craton, overriding plate); Yangtze, Yangtze craton (subducting plate); M, Moho discontinuity; A-A′ and B-B′, reflectors related to subduction of the Yangtze craton.

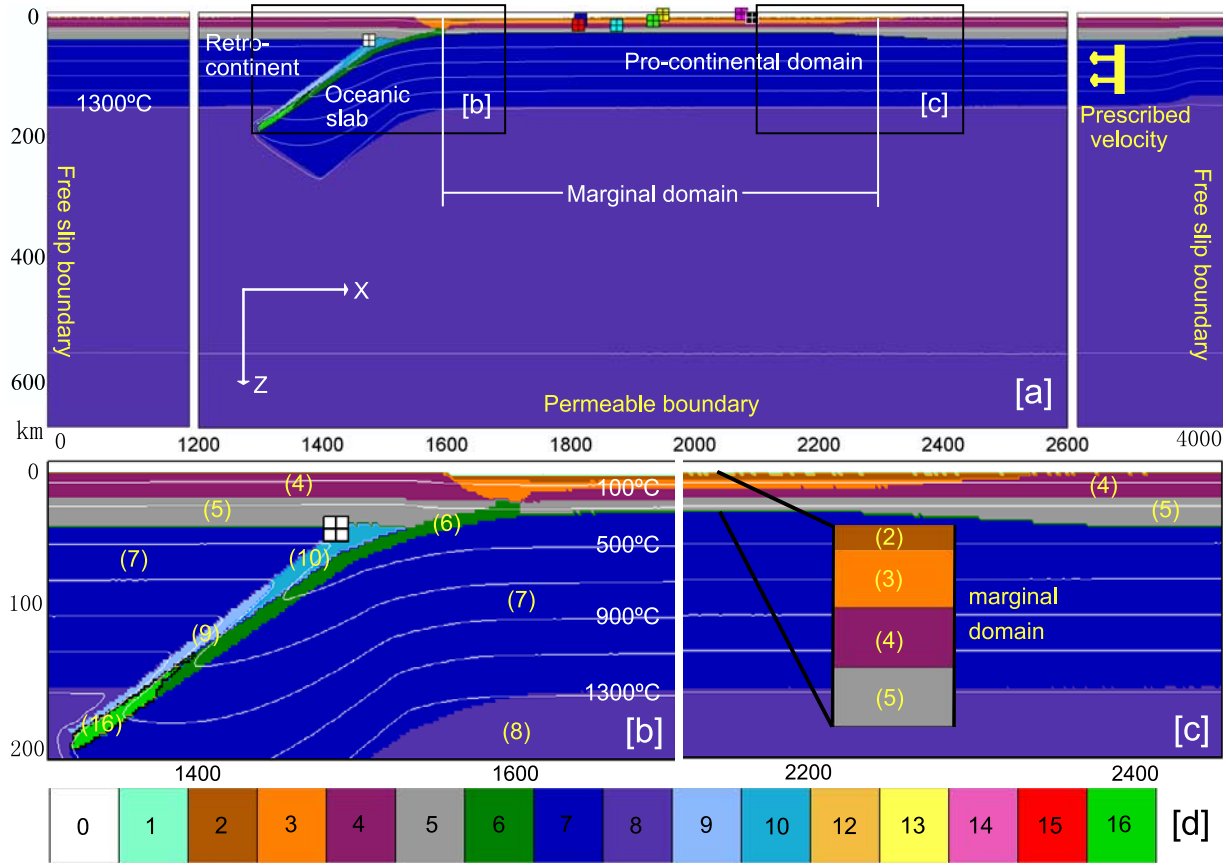

Figure 2. Initial model configuration and boundary conditions. (a) Enlargement (1400 × 670 km) of the numerical box (4000 × 670 km). Boundary conditions are indicated in yellow. Small colored squares (with pluses) indicate positions of representative markers (rock units) for P-T paths reconstruction (e.g., Figure 3). Colors of these squares are used for discrimination of marker points plotted in P-T diagrams and do not correspond to the colors of rock types (same in all the following experiments). (b and c) Zoomed domains corresponding to black rectangles in Figure 2a. Numbers shown in parentheses represent the rock types, referring to the color grid in Figure 2d. White lines are isotherms measured in °C. It is also necessary to note that there is no special meaning of the thin green line beneath the continental crust which is just produced in the visualization as the numerical interpolation between colors. (d) Color grid for different rock types, with 0, air; 1, water; 2,3, sediment; 4, upper continental crust; 5, lower continental crust; 6, oceanic crust; 7, lithospheric mantle; 8, athenospheric mantle; 9,10, hydrated and serpentinized mantle; 12,13, partially molten sediment (types 2 and 3); 14, partially molten upper continental crust (type 4); 15, partially molten lower continental crust (type 5); 16, partially molten oceanic crust (type 6). The partially molten continental crustal rocks (types 12, 13, 14, and 15) are not shown in Figure 2, which will appear during the evolution of the model (e.g., Figure 3). In our numerical models, the medium-scale layering usually shares the same physical properties, with different colors used only for visualizing slab deformation and structural development. This is the case for sediments and upper continental crust (types 2, 3, and 4), partially molten sediments and upper continental crust (types 12, 13, and 14), lithospheric and asthenospheric mantles (types 7 and 8), and hydrated and serpentinized mantles (types 9 and 10). Detailed properties of different rock types are shown in Table 1.

condition of 1.5–2.5 GPa and 500–600°C [*Zhang et al.*, 2002]; UHP 3 and 4, peak P-T conditions of P > 2.8 GPa [*Xu et al.*, 2006a] and probably even to P > 5.5 GPa [*F. L. Liu et al.*, 2006], with T = 650–800°C [*Xu et al.*, 2006a] and 739–866°C [*F. L. Liu et al.*, 2006].

3. Numerical Model Design

[14] For our numerical study we use the 2-D code I2VIS [*Gerya and Yuen*, 2003a] based on finite differences and marker-in-cell techniques which runs on the Brutus cluster of ETH-Zurich (see sections A1–A4 for details of numerical methodology). Large-scale models (4000 × 670 km, Figure 2a) are designed for the study of dynamic processes during continental subduction/collision associated with HP-UHP rocks formation and exhumation. The nonuniform 393 × 131 rectangular grid is designed with a resolution varying from 2 × 2 km in the studied collision zone to 30 × 30 km far away from it. Lithological structure of the model

is represented by around 7 million markers. The velocity boundary conditions (Figure 2a) are free slip at all boundaries except the open lower boundary along which an infinity-like mass conservative condition is imposed [*Gerya et al.*, 2008].

[15] In our numerical models, the driving mechanisms of subduction are combining the forces of ''plate push'' (prescribed leftward convergence velocity in a small internal domain that remains fixed with respect to the Eulerian coordinate, Figure 2a) and ''slab pull'' (temperature-induced density contrast between the subducted lithosphere and surrounding mantle). This type of boundary condition is applied widely in the numerical models of subduction and collision [e.g., *Toussaint et al.*, 2004a; *Burg and Gerya*, 2005; *Yamato et al.*, 2007; *Warren et al.*, 2008b; *Currie et al.*, 2007], assuming that in the globally confined three-dimensional system of plates, local ''external forcing'' imposed on a 2-D section of a plate and representing tectonic forces coming either from different slabs or from different sections of the same laterally nonuniform slab can be significant. Although slab pull is considered the most significant global 3-D driving force in subduction and it may be questioned why lateral plate push is a starting boundary condition in the models, removing this kind of lateral push from the 2-D model is not necessarily the most realistic option since in this case the plate will be driven only by the local negative buoyancy generated in exactly the same 2-D section. In contrast, 3-D plate motion is driven by the global negative buoyancy of the plate so that subduction does not always correlate with the local slab age and even ridges can be subducted [e.g., *Labrosse and Jaupart*, 2007]. Spontaneously growing slab pull in this type of 2-D models mainly regulates slab bending dynamics and delamination of the slab from the overriding plate [e.g., *Gerya et al.*, 2008].

[16] Following previous numerical studies performed with similar geodynamic settings [e.g., *Beaumont et al.*, 2006; *Warren et al.*, 2008a, 2008b; *Gerya et al.*, 2008] we designed numerical models consisting of three major domains (from right to left, Figure 2a): (1) a procontinental domain, (2) an oceanic domain, and (3) a retrocontinental domain. The subducting procontinent comprises a frontal or marginal unit (hereinafter referred to as the ''marginal domain'') and an interior unit. The marginal domain can be considered to represent rifted margin sediments, a formerly active continental margin, juvenile accreted terrane(s) or their combinations [e.g., *Warren et al.*, 2008a, 2008b], and/or an extended continental margin which may be as wide as 700 km [e.g., *Zhang and Shi*, 2003]. The interior unit represents stronger continental crust. Subduction of the marginal domain before actual collision between strong continental interiors strongly influences the regime of orogeny and exhumation of (U)HP rocks [e.g., *Warren et al.*, 2008a, 2008b; *Gerya et al.*, 2008]. Therefore, in contrast to the previous studies with limited 200–500 km width of the marginal domain, we varied this model parameter from 100 to 1700 km to systematically investigate influences of subducting large intervals of relatively thin (transitional) crust for metamorphic histories of (U)HP rocks. It is also worth noting that the largest/infinite width of marginal domain (1700 km) is not quite realistic in nature, which mainly contributes to demonstrate the ''end-member'' influences of this parameter.

[17] The initial material setup (Figures 2b and 2c) of our models implies transition from oceanic-continental subduction to collision: the oceanic crust (8 km in thickness) almost totally presubducted under the overriding plate, followed by the marginal domain which has relatively thin crust (24 km in thickness, with sedimentary layer, upper/middle crust, lower crust, each of 8 km) compared to the normal continental crust (35 km in thickness, with upper crust of 16 km and lower crust of 19 km). A relatively large width of hydrated mantle prescribed above the slab (Figure 2b) is related to the significant amount of water released from the slab during oceanic subduction [e.g., *Gerya et al.*, 2002; *Gerya and Stöckhert*, 2006]. The material properties of all layers (Figure 2) are shown in Table 1.

[18] The initial thermal structure (white lines in Figures 2a, 2b, and 2c) of the lithosphere is laterally uniform with zero horizontal heat flux across the vertical boundaries and corresponds to a usual continental geotherm [e.g., *Turcotte and Schubert*, 2002]: 0°C at the surface, and 1350°C at 150 km depth. The initial temperature gradient in the asthenospheric mantle is 0.5°C km^{-1}. For the lower boundary an infinity-like thermal condition is imposed [*Burg and Gerya*, 2005; *Gerya et al.*, 2008]. In the orogenic area of the model the lithospheric temperature profile is gradually bent downward along the shape of the subducting slab (Figure 2b).

4. Results

4.1. Reference Model

[19] Our reference model (Figure 3) chosen for comparing with the Sulu UHP terrane, corresponds to the experiment with 700 km width of the marginal domain, constant convergence velocity of 3.4 cm a^{-1}, and sedimentation and erosion rates both of 1.0 mm a^{-1} (model zhaa in Table 2).

[20] From the initial stage, the marginal domain is subducted into the forming crustal channel penetrating to 100–150 km depth. As the buoyancy force increases, the subducted sedimentary layer and upper/middle crust decouple from the lower crust and mantle (Figure 3a). Time of the decoupling is defined by the competing effects of crustal buoyancy (compared to the mantle) and subduction drag (related to rheological strength of the upper interface of subducting plate) [e.g., *Currie et al.*, 2007; *Faccenda et al.*, 2008]. Failure of the subducting crust results in forming of a rheologically weak zone (first detachment/thrust fault) at the entrance zone of subduction channel (Figures 3a and 3b; see also Figures 4–6 for detailed viscosity, strain rate and stress field evolution). In the following, detached part of subducted crustal rocks located in the upper part of subduction channel exhume toward shallower depths (<1 GPa, Figure 3c, first HP exhumation). In contrast, crustal rocks located in the lower part of the channel continue subducting and detach from the slab at asthenospheric depths, intruding into the mantle wedge and forming horizontal compositionally buoyant plume (Figures 3b and 3c). The viscosity of both the sublithospheric plume and the surrounding mantle, which has the temperature of up to 900°C, is relatively low (10^{19}–10^{21} Pa s; Figure 4) allowing efficient horizontal spreading

Table 1. Material Properties Used in Numerical Experiments

Material	State	ρ_0 (kg m^{-3})	k (W m^{-1} K^{-1})	$T_{solidus}$ (K)	$T_{liquidus}$ (K)	Q_L (kJ kg^{-1})	Hr (μW m^{-3})	Flow Law	E (kJ mol^{-1})	n	A_D (MPa^{-n} s^{-1})	V (J MPa^{-1} mol^{-1})
Sediment and continental crust	Solid (2,3) (4,5)[a]	2700[b]	$[0.64 + 807/(T_K + 77)]$ $\exp(0.00004P_{MPa})$	$889 + 17900/(P + 54)$ $+ 20200/(P + 54)^2$ at P<1200 MPa $831 + 0.06P$ at P>1200 MPa	$1262 + 0.09P$	300	2.0 for (2,3,4,12 13,14)[a] 0.5 for (5,15)[a]	Strong[c] wet quartzite	154	2.3	$10^{-6.5}$	0
	Molten (12,13) (14,15)[a]	2500						-	0	1	$10^{-8.7}$	0
Oceanic crust	Solid (6)[a]	3300	$[1.18 + 474/(T_K + 77)]$ $\exp(0.00004P_{MPa})$	$973 - 70400/(P + 354)$ $+ 778 \times 10^5/(P + 354)^2$ at P < 1600 MPa $935 + 0.0035P +$ $0.0000062P^2$ at P > 1600 MPa	$1423 + 0.105P$	380	0.25	Plagioclase An_{75}	238	3.2	$10^{-3.5}$	0
	Molten (16)[a]	2900						-	0	1	10^{-7}	0
Lithospheric-athenospheric mantle	Dry (7,8)[a]	3300	$[0.73 + 1293/(T_K + 77)]$ $\exp(0.00004P_{MPa})$	-	-	-	0.022	Dry Olivine	532	3.5	$10^{4.4}$	8
	Hydrated (9,10)[a]	3000–3300		-	-	-	0.022	Wet Olivine	470	4	$10^{3.3}$	8
References[d]		1,2	3	4	4	1,2	1	5	5	5	5	1,5

[a]Numbers of materials are corresponding to Figure 2. The parameters are $\alpha = 3 \times 10^{-5}$ K^{-1}, $\beta = 1 \times 10^{-5}$ MPa^{-1} for all rock types, Cp = 1000 J kg^{-1} K^{-1} for all "solid" rock types and Cp = 1500 J kg^{-1} K^{-1} for "molten" rock types.

[b]The value 3000 kg m^{-3} is used for the investigation of changeable convergence conditions.

[c]The "strong" wet quartzite flow law is implemented by decreasing the A_D value by a factor of 10^3 relative to the normal wet quartz flow law.

[d]References are 1, *Turcotte and Schubert* [1982]; 2, *Bittner and Schmeling* [1995]; 3, *Clauser and Huenges* [1995]; 4, *Schmidt and Poli* [1998]; 5, *Ranalli* [1995].

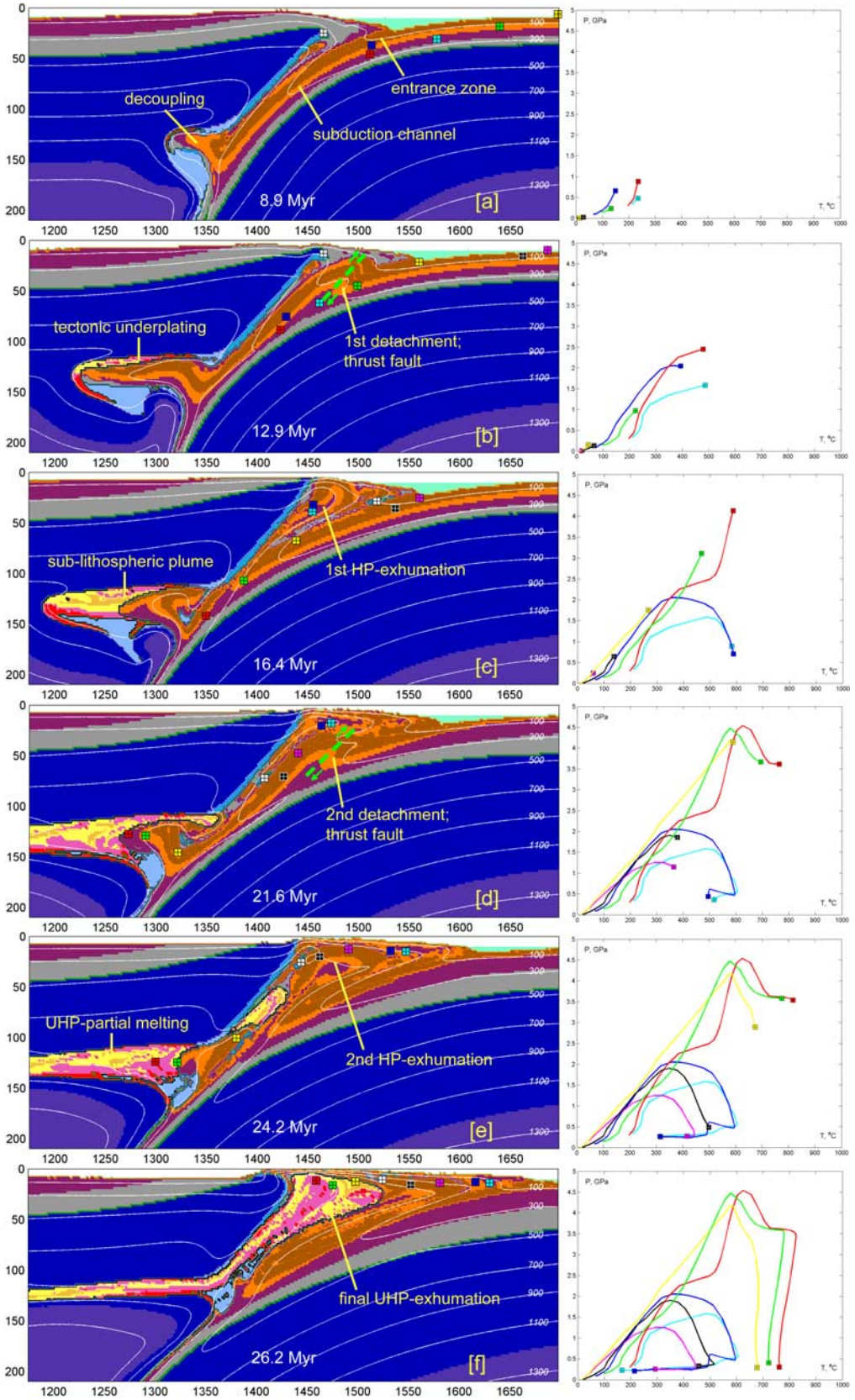

Figure 3. Evolution of the reference model (model zhaa in Table 2) within enlarged 500 × 210 km domain of the original 4000 × 670 km model. Colors of rock types are as in Figure 2. Time (Ma) of shortening is given. White numbered lines are isotherms in °C. P-T paths for positions of representative markers (rock units) which are indicated by small colored squares (with pluses). The selected markers are the same as in Figure 2.

Table 2. Variable Parameters of Numerical Experiments

Experiments	Margin Width (km)	Convergence Velocity (cm a^{-1})	Sedimentation Rate (mm a^{-1})	Erosion Rate (mm a^{-1})	t_{stop} (Ma)	t_{zero} (Ma)
zhaa[a]	700[a]	3.4[a]	1.0[a]	1.0[a]	NU[a]	NU[a]
zhba	100	RP[b]	RP[b]	RP[b]	RP[b]	RP[b]
zhbb	300	RP[b]	RP[b]	RP[b]	RP[b]	RP[b]
zhbc	500	RP[b]	RP[b]	RP[b]	RP[b]	RP[b]
zhbd	900	RP[b]	RP[b]	RP[b]	RP[b]	RP[b]
zhbe	1700 (inf)	RP[b]	RP[b]	RP[b]	RP[b]	RP[b]
zhca	RP[b]	1.0	RP[b]	RP[b]	RP[b]	RP[b]
zhcb	RP[b]	2.0	RP[b]	RP[b]	RP[b]	RP[b]
zhcc	RP[b]	5.0	RP[b]	RP[b]	RP[b]	RP[b]
zhcd	RP[b]	6.5	RP[b]	RP[b]	RP[b]	RP[b]
zhda	RP[b]	RP[b]	0.3	RP[b]	RP[b]	RP[b]
zhdb	RP[b]	RP[b]	3.0	RP[b]	RP[b]	RP[b]
zhdc	RP[b]	RP[b]	RP[b]	0.3	RP[b]	RP[b]
zhdd	RP[b]	RP[b]	RP[b]	3.0	RP[b]	RP[b]
zhde	RP[b]	RP[b]	0.3	0.3	RP[b]	RP[b]
zhdf	RP[b]	RP[b]	3.0	3.0	RP[b]	RP[b]
zhea[c]	RP[b]	RP[b]	RP[b]	RP[b]	5.0	RP[b]
zheb[c]	RP[b]	RP[b]	RP[b]	RP[b]	7.5	RP[b]
zhec[c]	RP[b]	RP[b]	RP[b]	RP[b]	10.0	RP[b]
zhed[c]	RP[b]	RP[b]	RP[b]	RP[b]	RP[b]	7.5
zhee[c]	RP[b]	RP[b]	RP[b]	RP[b]	RP[b]	15.0
zhef[c]	RP[b]	5.0	RP[b]	RP[b]	RP[b]	7.5
zheg[c]	RP[b]	5.0	RP[b]	RP[b]	RP[b]	15.0
zheh[c]	RP[b]	6.5	RP[b]	RP[b]	RP[b]	7.5
zhei[c]	RP[b]	6.5	RP[b]	RP[b]	RP[b]	15.0

[a]The reference model and reference parameters. The meanings of t_{stop} and t_{zero} are shown in Figures 13a and 14. NU indicates that the changeable convergence conditions (t_{stop} or t_{zero}) are not used. All the other parameters of the numerical experiments are shown in Table 1.
[b]RP, values same as the reference parameters.
[c]Relatively longer oceanic slab and higher density of continental crustal materials (3000 kg m^{-3}) are used.

of crustal rocks under the colder and stronger mantle lithosphere. Such sublithospheric crustal plumes are studied systematically by *Currie et al.* [2007] which indicated that underplating behavior is favored by lowered density and viscosity and increased thickness of subducted crustal layer.

[21] The continental crust continues subducting during and after the first HP exhumation episode until another rheologically weak zone forms (second detachment/thrust fault) (Figure 3d), followed by the second exhumation of HP rocks (Figure 3e). This second exhumation episode is similar to the first one, with the subducted crustal rocks from the upper part of subduction channel exhuming toward shallower depths (<1 GPa, Figure 3e) while crustal rocks forming lower part of the channel continue subducting with forming the sublithospheric plume (Figures 3d and 3e).

[22] Exhumation of UHP metamorphic rocks from the sublithospheric plume occurs after the second HP exhumation episode (Figure 3f). It takes about 4 Ma for these UHP rocks to move from sublithospheric depths to the crustal levels and to distribute near the suture zone. Long (several million years) residence time of crustal rocks in the sublithospheric plume associated with strong conductive heating from the underlying asthenospheric mantle results in high peak temperatures of 800–850°C at UHP conditions (Figures 3e and 3f).

[23] Our reference model thus predicts three different phases of detachment/exhumation processes differing in P-T peak metamorphic conditions (time elapsed from the beginning of the experiment is given for these phases): (1) 12–16 Ma, first thrust fault formation and first HP rocks exhumation, with P-T conditions of about 1.5–2.5 GPa and 500–600°C (Figure 3c); (2) 20–24 Ma, second thrust fault formation and second HP rocks exhumation, with P-T conditions of about 1–2.5 GPa and 400–500°C (Figure 3e); and (3) 22–26 Ma, exhumation of the UHP-HT rocks from the sublithospheric plume, with P-T conditions of 4–5 GPa and 700–800°C (Figure 3f).

[24] Peak metamorphic temperatures for HP rocks exhumed during the second episode (black and pink P-T paths, Figures 3e and 3f) are somewhat lower (~100°C) than for the first episode (dark blue and light blue P-T paths, Figures 3e and 3f). That is because the continued subduction of cold rocks decreases the temperature conditions in the subduction channel. On the other hand, significant temperature increase (from 600 to 800°C) after peak pressure conditions is recorded for UHP rocks forming the sublithospheric plume (red and green P-T paths, Figures 3e and 3f).

4.2. Variable Width of Marginal Domain

[25] We conducted experiments with marginal domain width of 100, 300, 500, 700 (reference), 900, and 1700 (“infinite”) kilometers (Table 2).

[26] In the experiments with relatively narrow marginal domain (model zhbb in Table 2), this domain subducts and forms the sublithospheric plume (Figures 7a and 7b) similar to the reference model. Then the subducting thick continental interior collides with the overriding plate (Figures 7c and 7d), with the subduction channel being closed in the upper section. Consequently, the exhumation processes of subducted rocks cannot proceed toward the surface as in the reference model. These rocks are instead accumulated in the crustal wedge formed under the collision belt (Figure 7e). This implies that narrow width of the marginal domain is

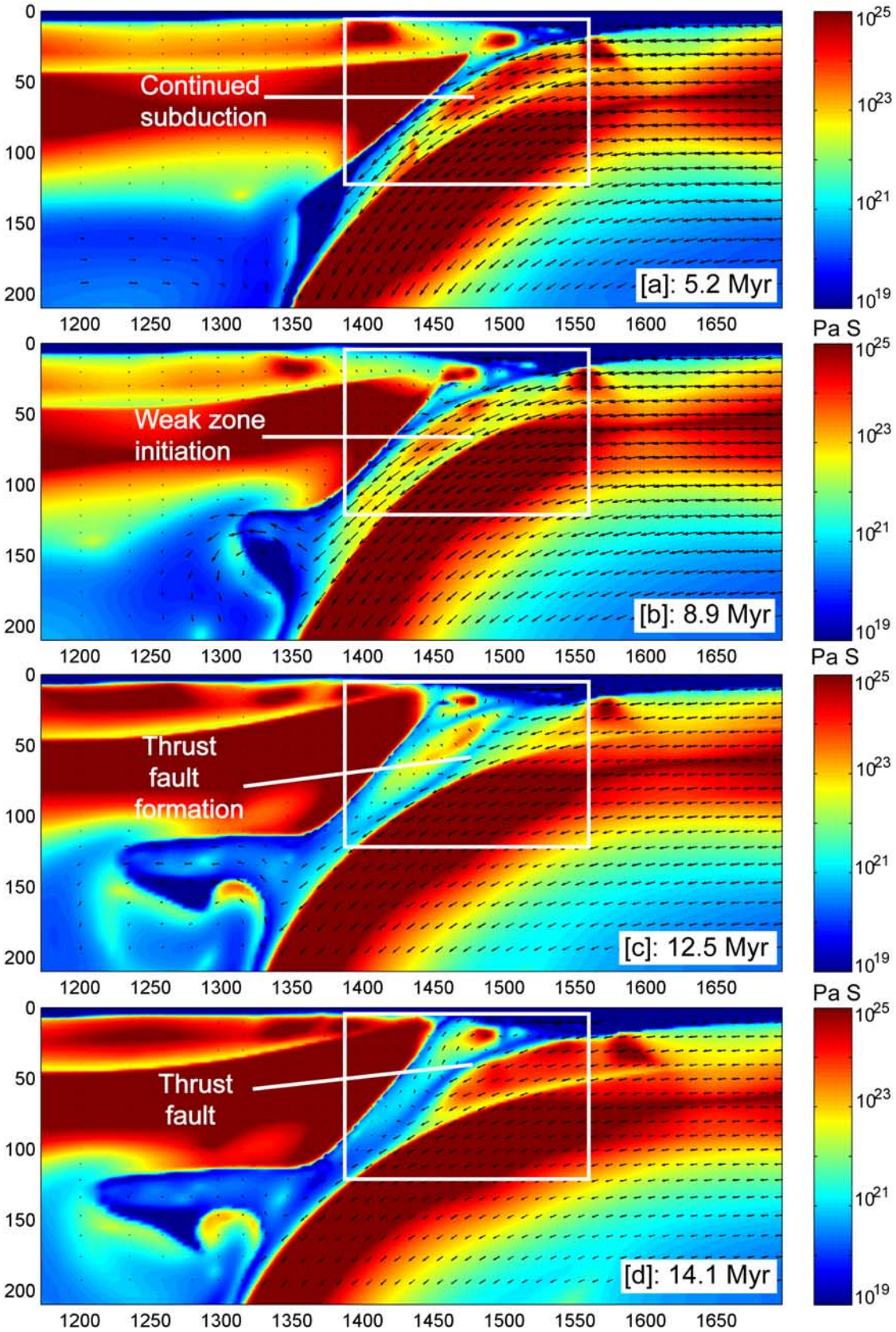

Figure 4. Effective viscosity field for the reference model (Figure 3) within enlarged 500 × 210 km domain of the original 4000 × 670 km model. Black arrows show the calculated velocity field. Colors represent the magnitude of effective viscosity (as in the color bar). Time (Ma) of shortening is given. White rectangles outline area of interest close around the subduction channel.

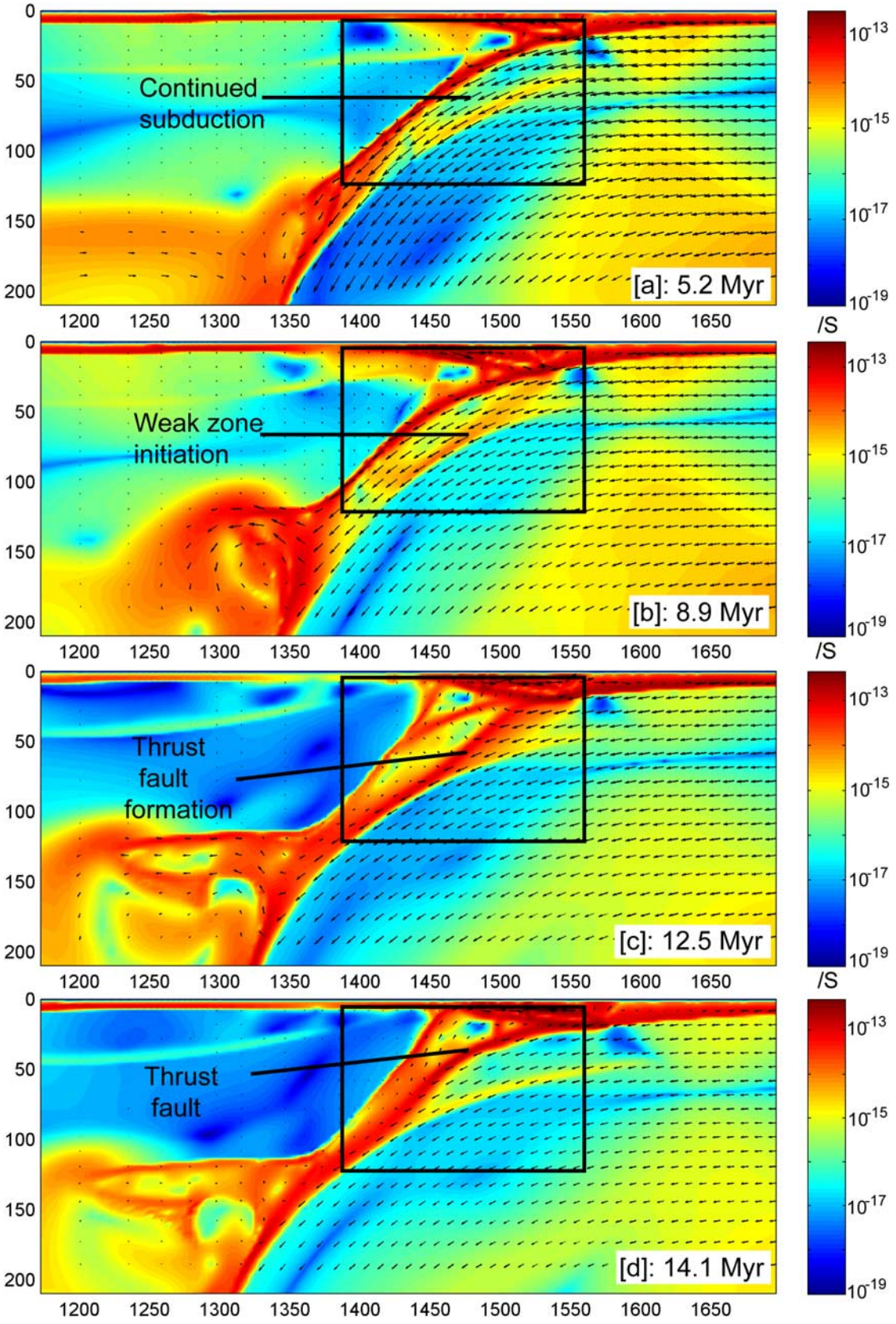

Figure 5. Second invariant of deviatoric strain rate field (ε_{II}) for the reference model (Figure 3) within enlarged 500 × 210 km domain of the original 4000 × 670 km model. Black arrows show the calculated velocity field. Colors represent the magnitude of ε_{II} (as in the color bar). Time (Ma) of shortening is given. Black rectangles outline area of interest close around the subduction channel.

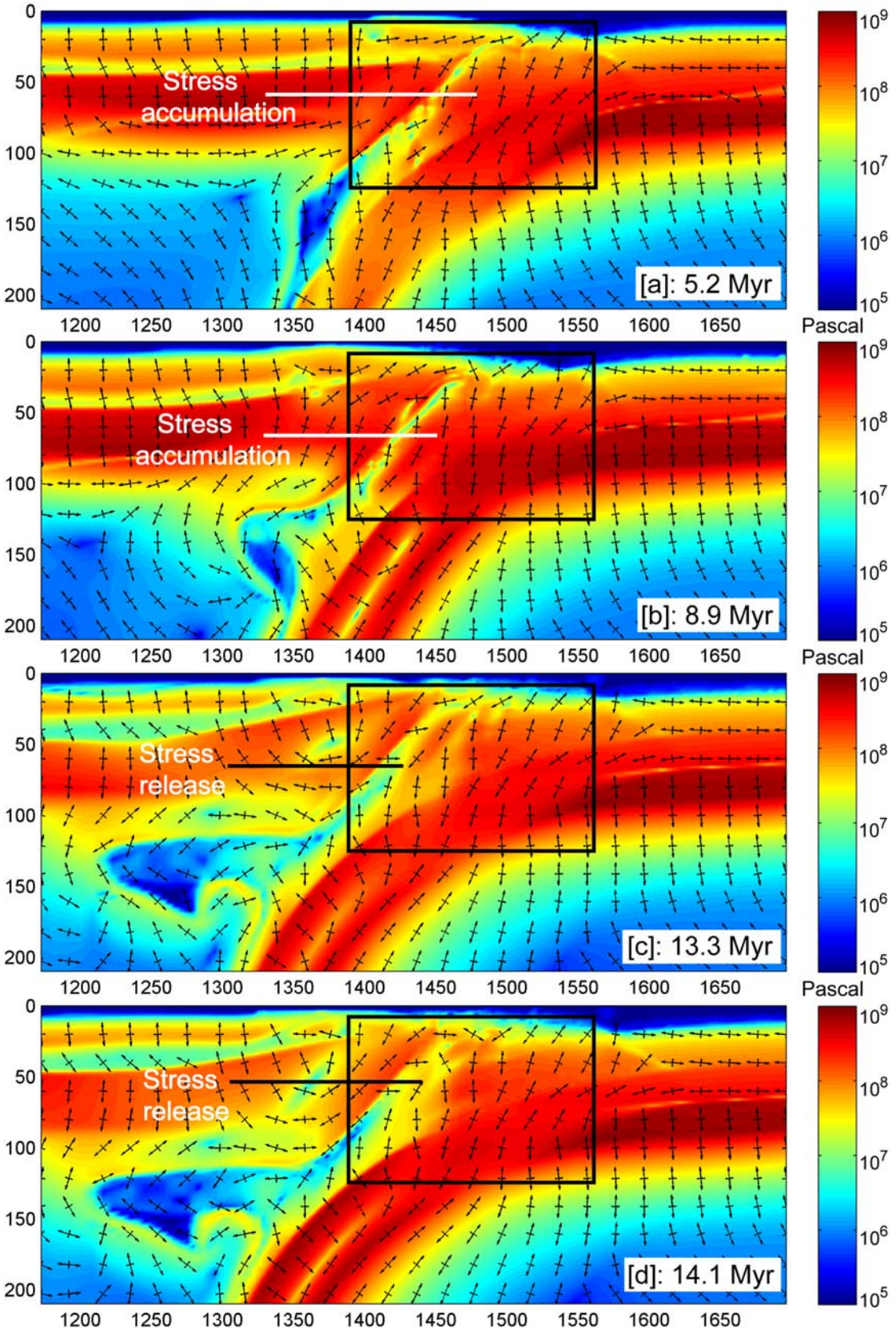

Figure 6. Second invariant of deviatoric stress field (σ_{II}) for the reference model (Figure 3) within enlarged 500 × 210 km domain of the original 4000 × 670 km model. Black crosses show the directions of the principal stresses, with the longer arrows for σ_3 (extension) and shorter arrows for σ_1 (compression). Colors represent the magnitude of σ_{II} (as in the color bar). Time (Ma) of shortening is given. Black rectangles outline area of interest close around the subduction channel.

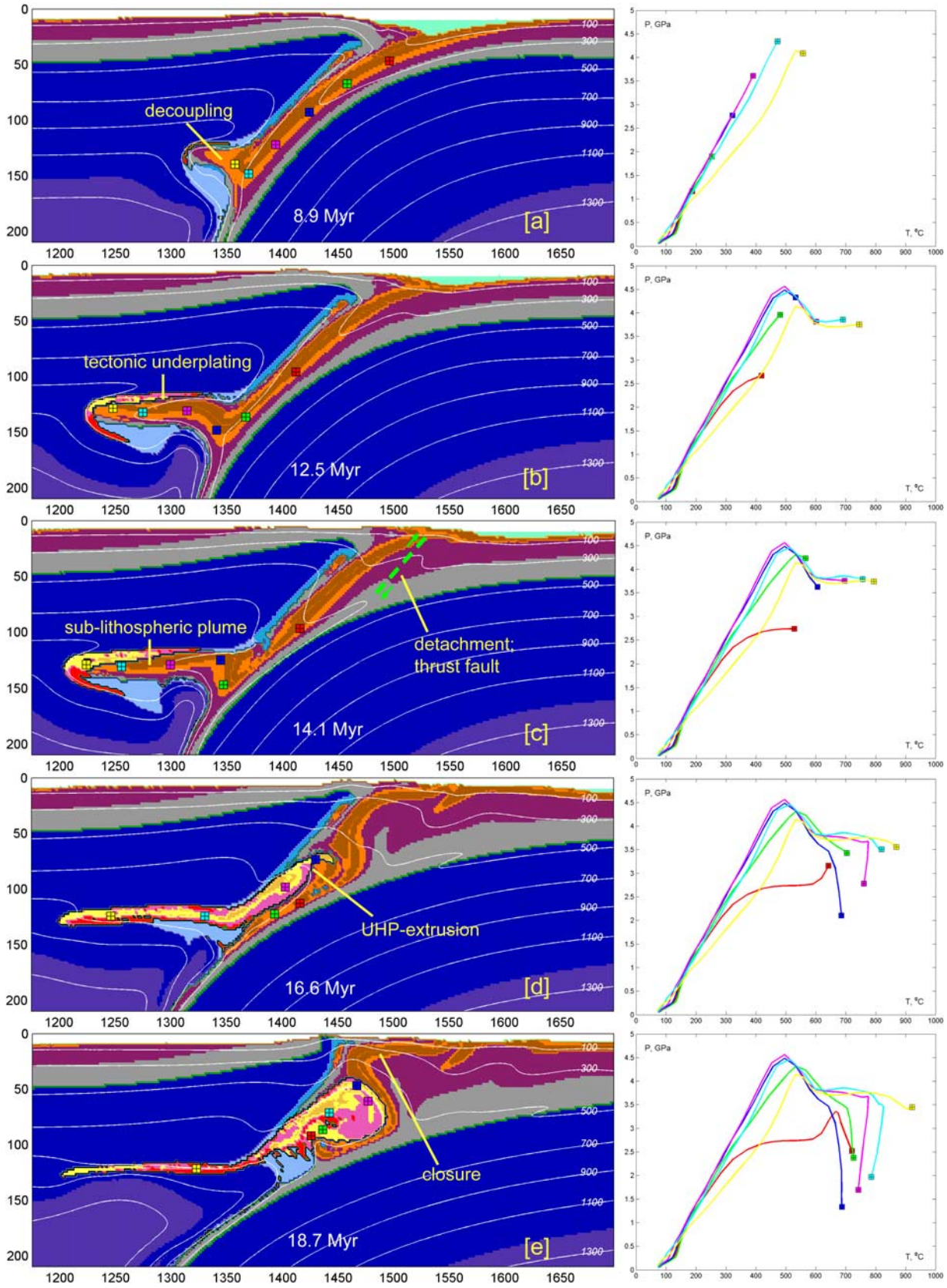

Figure 7. Evolution of the model with smaller (300 km) marginal domain (model zhbb in Table 2) within enlarged 500 × 210 km domain of the original 4000 × 670 km model. Colors of rock types are as in Figure 2. Time (Ma) of shortening is given in the figures. White numbered lines are isotherms in °C. P-T paths for positions of representative markers (rock units) which are indicated by small colored squares (with pluses).

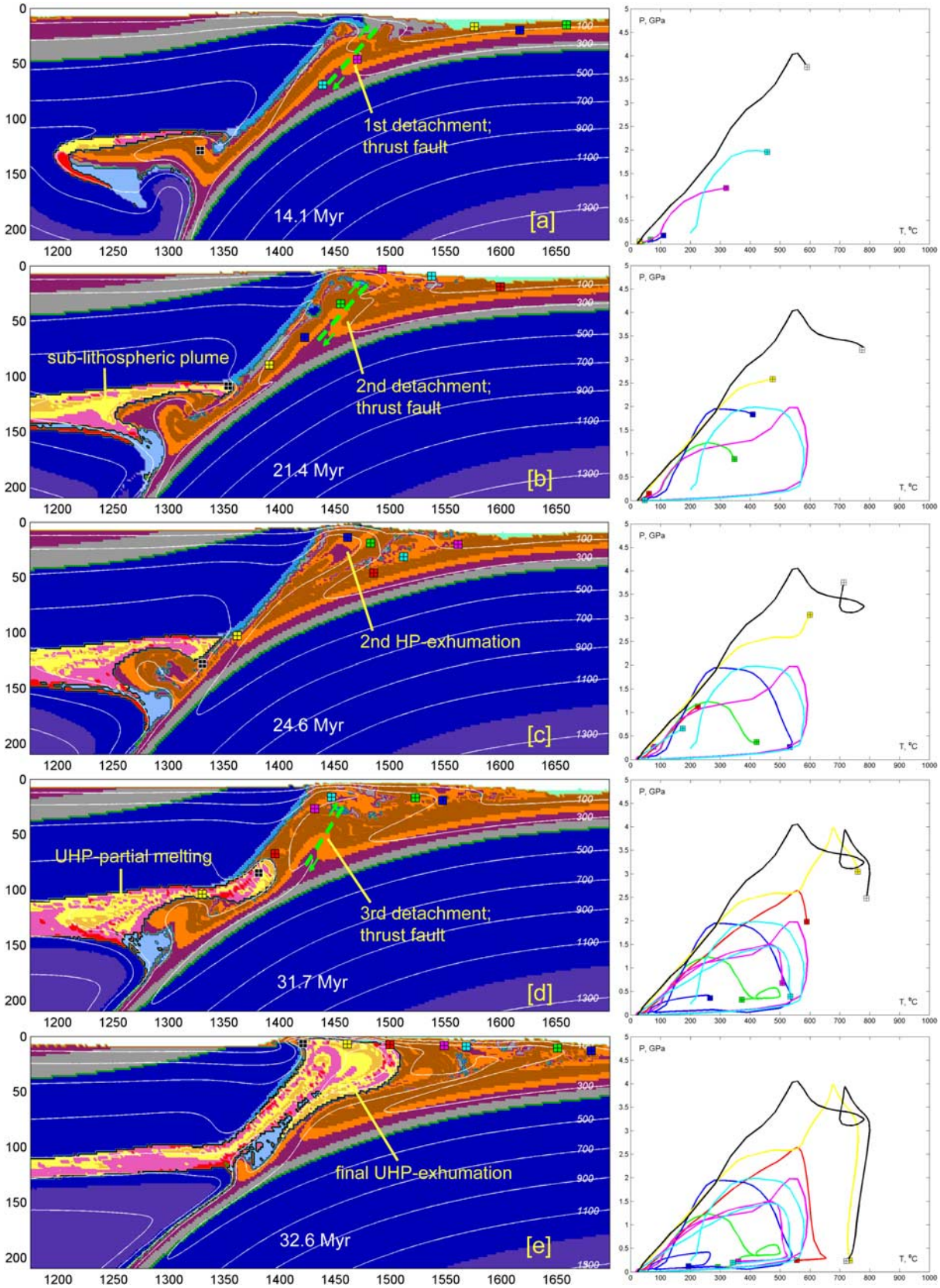

Figure 8. Evolution of the model with larger (1700 km, infinite) marginal domain (model zhbe in Table 2) within enlarged 500 × 210 km domain of the original 4000 × 670 km model. Colors of rock types are as in Figure 2. Time (Ma) of shortening is given in the figures. White numbered lines are isotherms in °C. P-T paths for positions of representative markers (rock units) which are indicated by small colored squares (with pluses).

not favorable for triggering efficient UHP rocks exhumation to the surface.

[27] In the experiments with wide marginal domain (model zhbe in Table 2), the "first" (Figure 8a) and "second" (Figure 8b) thrust fault formation associated with HP rocks exhumation processes is similar to the reference model (Figures 3b and 3d). However, the UHP rocks do not exhume after the second HP exhumation episode. Instead the marginal domain continues subducting (Figure 8c) until the "third" thrust fault forms (Figure 8d), being followed by the UHP-HT rocks exhumation from the sublithospheric plume (Figure 8e).

4.3. Variable Convergence Velocity

[28] We have tested (Table 2) both low (1.0, 2.0 cm a^{-1}) and high (5.0, 6.5 cm a^{-1}) convergence velocity compared to the reference model (3.4 cm a^{-1}).

[29] With the low convergence velocity of 2.0 cm a^{-1} (Figure 9), the subducted crustal rocks cannot underplate the overriding lithosphere since subduction drag is small compared to buoyancy forces [e.g., *Raimbourg et al.*, 2007; *Warren et al.*, 2008b]. After reaching the UHP depth of ~100 km, the thrust fault forms at the entrance zone of subduction channel (Figure 9a), being followed by the exhumation of both HP (Figure 9b) and UHP (Figure 9c) rocks. Then the marginal domain continues subduction with circulation of exhumed rocks in the wedge-like subduction channel confined between two plates (Figure 9d), which gets shallower with time and finally closes. During this process subducted crustal rocks are thrust over the overriding plate (Figure 9e). In the experiment with even lower (1.0 cm a^{-1}) convergence velocity (model zhca in Table 2) marginal domain only subducts to HP depth of around 50 km.

[30] In the high convergence velocity regime (5.0 cm a^{-1}; Figure 10) when subduction drag strongly dominates over the buoyancy forces, the marginal domain continues subduction with the crustal rocks detaching and forming the sublithospheric plume (Figures 10a and 10b) until almost the entire marginal domain (~700 km) is subducted. Then the 35 km thick interior section of the subducting crust collides with the overriding plate with the UHP-HT rocks extruding into the bottom of the thick and wide wedge-like collision zone (Figures 10d and 10e). Higher convergence velocity of 6.5 cm a^{-1} produces compressional instabilities (e.g., buckling, folding) in the lithosphere [e.g., *Toussaint et al.*, 2004b; *Agard et al.*, 2007].

4.4. Variable Sedimentation and Erosion Rates

[31] The variations in sedimentation and erosion rates do not change the polyphase character of subduction-detachment-exhumation processes and only affect (1) the formation time of the first thrust fault (Figure 11) and (2) the size and exhumation time of the UHP rocks (Figure 12).

[32] Lower sedimentation and/or erosion rates (Figures 11a and 11b) delay the formation of the first fault while higher rates (Figures 11d and 11e) accelerate this process compared to the reference model (Figure 11c). Mechanisms of erosion and sedimentation influences are indeed different. Higher sedimentation rate produces more buoyant sediments subducted into the channel which causes higher buoyancy accumulation rate leading to detachment. In contrast higher erosion rate rapidly removes rocks from the elevated region of the overriding plate atop the hanging wall of subduction channel thus facilitating onset of the return flow in the channel associated with detachment.

[33] Erosion rate plays an important role in the final UHP exhumation processes: in the lower erosion rate regime the exhumation of UHP rocks occurs later (Figure 12b); while higher erosion rate produces (Figure 12e) earlier exhumation and smaller size of exhuming partially molten UHP rock unit (exhumation focusing [*Ellis et al.*, 1999; *Gerya et al.*, 2008]). In contrast, sedimentation rate does not influence timing for the final exhumation of the UHP rocks (compare Figures 12a, 12c, and 12d) and only affects size and shape of exhumed rock units.

4.5. Variable Convergence Condition

[34] We test possible influences of the convergence condition (1) by prescribing constant convergence velocity (v_{x0}) from the beginning of experiment to a certain time point (t_{stop}, Figure 13a) after which the model evolves spontaneously under the slab pull and (2) by prescribing convergence velocity decreasing linearly with time from an initial value (v_{x0}) to zero at a certain time point (t_{zero}, Figure 14) after which both plates remain fixed with no convergence. In these experiments we also created stronger slab pull by increasing the length of presubducted oceanic slab (compare Figures 13a and 2a) and the density of continental crust and sediments (3000 kg m^{-3} compared to 2700 kg m^{-3} in the reference model, Table 1).

[35] Figure 13 shows the results of experiment (model zheb in Table 2) with prescribing constant convergence velocity of 3.4 cm a^{-1} from the beginning of the experiment and then removing this condition at 7.5 Ma (t_{stop}). After the cancellation of the prescribed velocity, the continental crustal rocks continue subduction at slower rate of about 1 cm a^{-1} (Figure 13a). This is followed by decoupling of the continental crust from the slab and forming relatively small sublithospheric plume (compare Figures 13c and 3e). And then thrust fault forms in the subduction channel (Figure 13c) with the exhumation of HP and then UHP rocks and the athenopheric upwelling (Figures 13c and 13d). The subduction channel gets progressively wider and shallower with the continued subduction driven entirely by the slab pull (Figure 13e).

[36] The experiments with linearly decreasing convergence velocity demonstrate strong dependence of results on the prescribed length ($L = 1/2\ v_{x0} \times t_{stop}$) and average velocity ($1/2v_{x0}$) of convergence (Figure 14). Longer and faster convergence favors deeper continental subduction and sublithospheric plume formation (Figures 14d and 14f) while shorter and slower convergence results in relatively shallow continental subduction and no pronounced sublithospheric plume (Figures 14a and 14c). Also, all models with decreasing convergence rate result in notable delamination of the slab from the overriding plate associated with widening of the subduction channel and asthenospheric mantle upwelling (Figure 14). These features are direct consequences of significant slab pull and positive buoyancy of subducted continental crust composing the channel. Similar to the reference model UHP rocks typically form and exhume along the hanging wall of the subduction

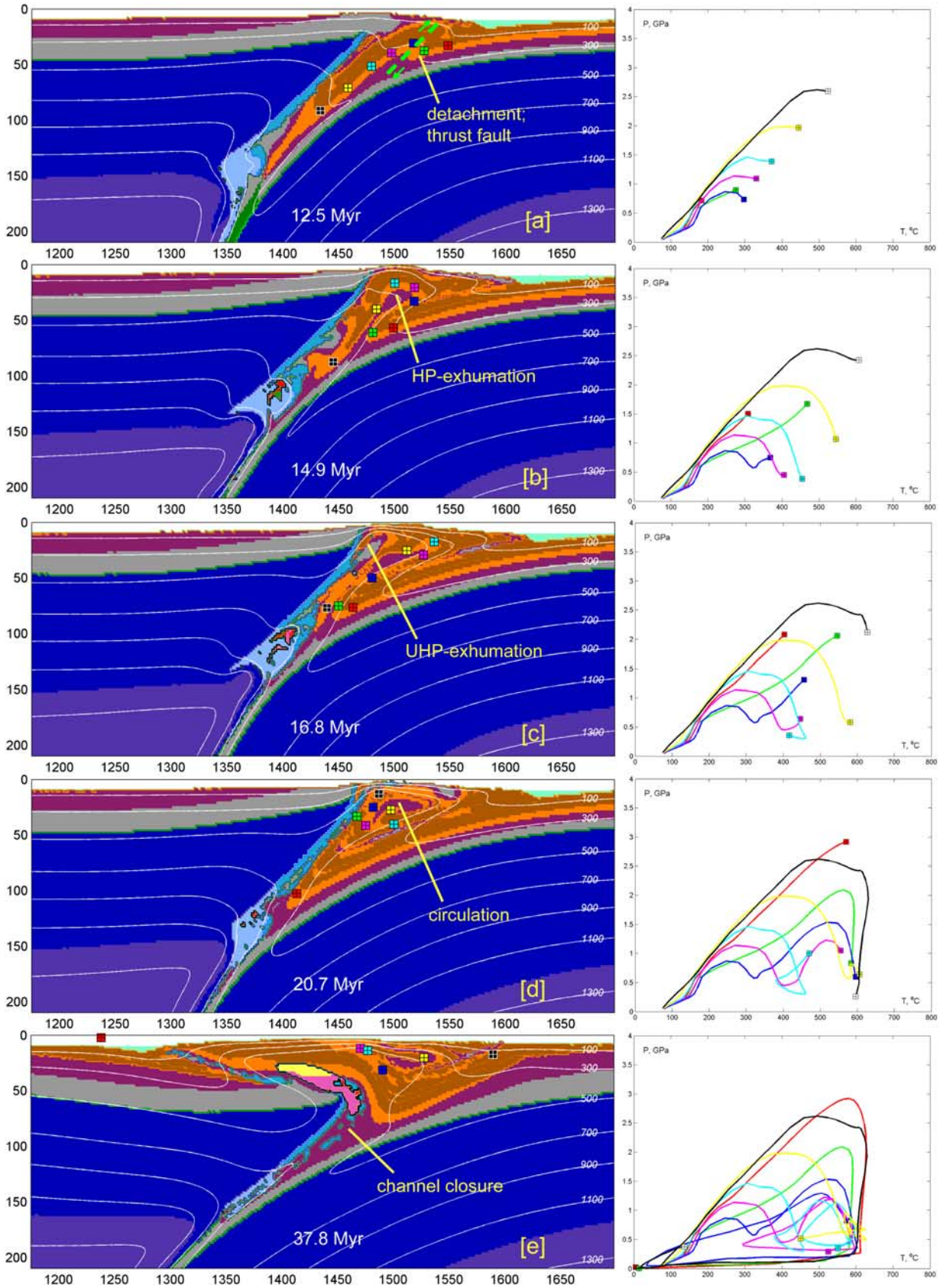

Figure 9. Evolution of the model with lower (2.0 cm a^{-1}) convergence velocity (model zhcb in Table 2) within enlarged 500 × 210 km domain of the original 4000 × 670 km model. Colors of rock types are as in Figure 2. Time (Ma) of shortening is given. White numbered lines are isotherms in °C. P-T paths for positions of representative markers (rock units) which are indicated by small colored squares (with pluses).

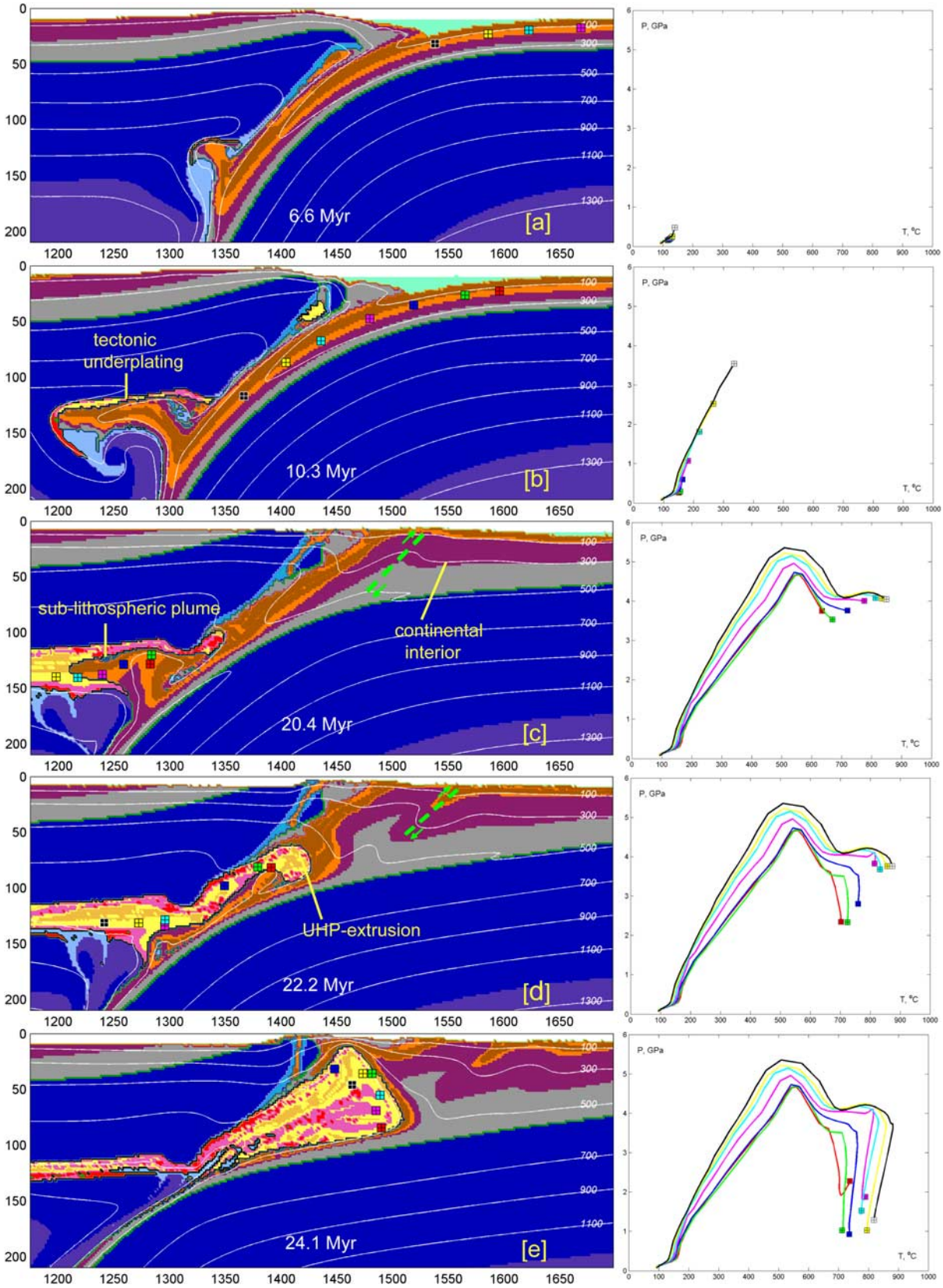

Figure 10. Evolution of the model with higher (5.0 cm a^{-1}) convergence velocity (model zhcc in Table 2) within enlarged 500 × 210 km domain of the original 4000 × 670 km model. Colors of rock types are as in Figure 2. Time (Ma) of shortening is given in the figures. White numbered lines are isotherms in °C. P-T paths for positions of representative markers (rock units) which are indicated by small colored squares (with pluses).

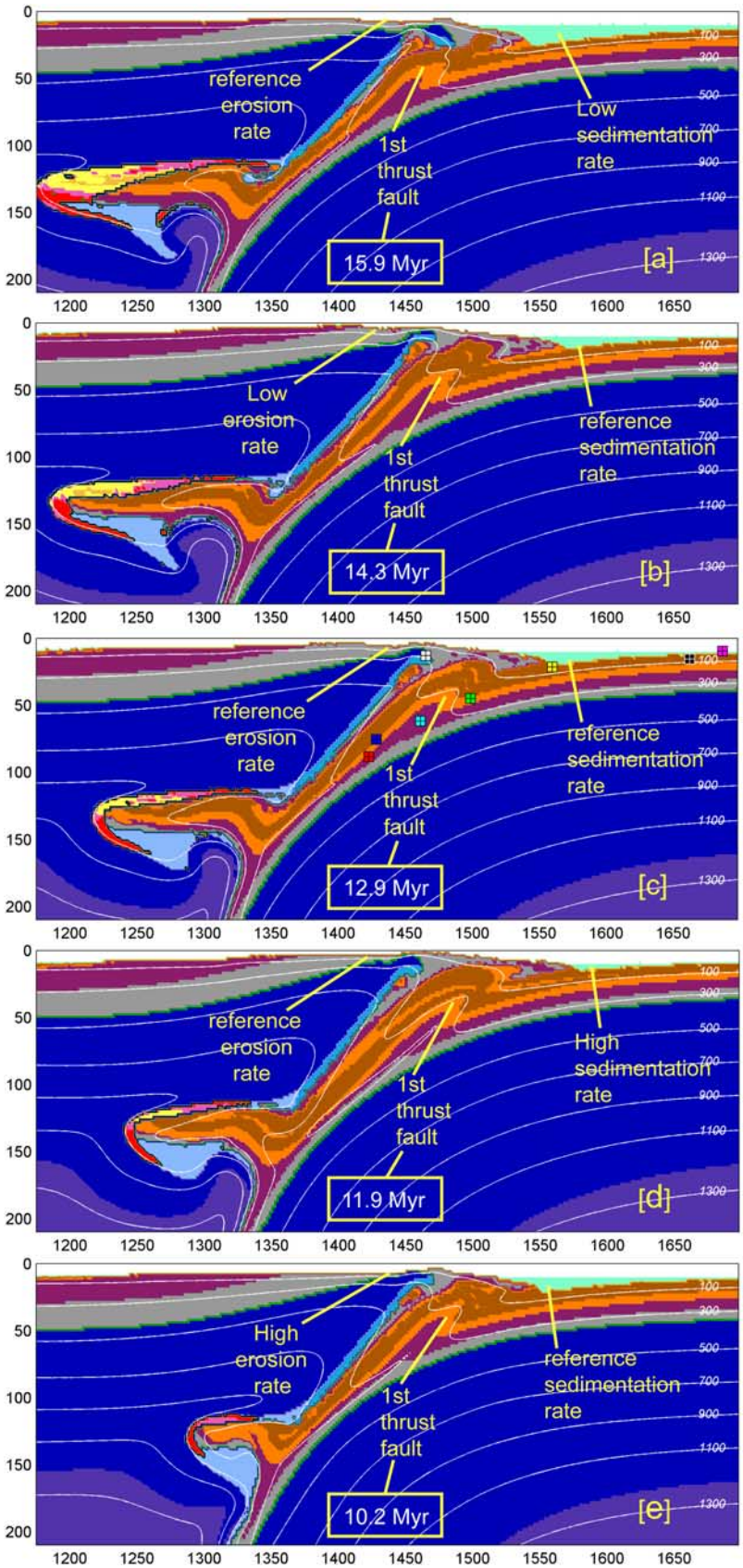
reference erosion rate
1st thrust fault
Low sedimentation rate
15.9 Myr
[a]
Low erosion rate
1st thrust fault
reference sedimentation rate
14.3 Myr
[b]
reference erosion rate
1st thrust fault
reference sedimentation rate
12.9 Myr
[c]
reference erosion rate
1st thrust fault
High sedimentation rate
11.9 Myr
[d]
High erosion rate
1st thrust fault
reference sedimentation rate
10.2 Myr
[e]
0
50
100
150
200
1200 1250 1300 1350 1400 1450 1500 1550 1600 1650
100
300
500
700
900
1100
1300

Figure 11

channel and their exhumation is always late compared to the exhumation of HP rocks.

5. Comparison of the Reference Model With Sulu UHP Terrane

[37] In our reference model, the exhumed HP-UHP rocks juxtapose in the collision belt, with the UHP metamorphic slices (Figure 15a, red) located near the suture zone and HP slices (Figure 15a, green-blue) away from it. The maps of peak metamorphic pressure (Figure 15a) and temperature (Figure 15c) conditions as well as distribution of different rock types (Figure 15e) indicate clearly presence of different exhumed tectonometamorphic slices experienced different degrees of HP-UHP metamorphism. On the basis of the peak P-T conditions (Figures 15a and 15c) and the lithological field (distribution of rock types, Figures 3 and 15e), the simulated exhumed metamorphic terrane can be subdivided into the following sections (Figure 15e): section I, HP slices with peak P-T conditions of 1.5–2.5 GPa and 500–600°C (phase 1, first exhumation); section II, HP slices with peak P-T conditions of 1–2.5 GPa and 400–500°C (phase 2, second exhumation); and sections III and IV, UHP slices with peak P-T conditions of 4–5 GPa and 700–800°C (phase 3, final exhumation).

[38] Simulated metamorphic and lithological zoning pattern is to a first order similar to the Sulu terrane (compare Figures 15e and 15f). Moreover, in the UHP domain the crustal metamorphosed rocks (pink and red in Figure 15e) mainly locate near the suture zone (UHP IV), which can be deciphered as the UHP in the Sulu terrane (Figure 15f), while the sedimentary metamorphosed rocks (yellow in Figure 15e, section III) can be deciphered as the UHP 3 in the Sulu terrane (Figure 15f).

[39] The peak P-T conditions of HP slices (HP I and II as a whole) are of 1–2.5 GPa and 400–600°C (Figures 15a, 15c, and 16, blue lines). These conditions are in agreement with the Sulu HP 2 and VHP 2 as a whole (Figure 16, rectangles). The simulated peak P-T conditions of UHP terranes (Figure 16, red lines) are consistent with the Sulu UHP slices (Figure 16, rectangle). Generally, such high-temperature conditions are related to the long residence time of UHP rocks in the sublithospheric plume (Figure 3).

[40] Distributions of relative ages (Figures 15b and 15d) at which peak pressure and peak temperature conditions were achieved are notably different from each other reflecting variations in geometry of characteristic P-T paths (Figure 16) for different rock units. The timescale maps (Figures 15b and 15d) of peak metamorphic conditions show that the peak metamorphism of "slices II, III, and IV" forms almost simultaneously, although the "core" of "UHP IV" is formed earlier reflecting long residence time of UHP rocks in the sublithospheric plume (Figure 3). In contrast, "slice I" experiences peak metamorphic conditions about 10 Ma earlier than the other parts indicating the temporal discrepancy between HP and UHP slices in the Sulu terrane.

[41] In the numerical model, the mixed rock types are mainly metamorphic sediments (yellow in Figure 15e) and upper/middle crustal rocks (pink in Figure 15e), with small amounts of partially molten lower crustal rocks (red in Figure 15e) and mantle rocks (dark blue in HP II section of Figure 15e). In addition, the protoliths are mainly from the subducted continental margin. They agree well with the lithological characteristics of the Sulu UHP terrane.

[42] Many of the models presented in this study, including the reference model, show significant amounts of overriding plate mantle exhumation and erosion. This tendency is mainly related to the up bending of the overriding plate during subduction and collision which is discussed in details by *Faccenda et al.* [2008] and compared to available natural examples. Large and possibly unrealistic amount of up bending of the overriding lithospheric mantle in our models may be related [*Faccenda et al.*, 2008] to the chosen relatively strong rheology of the overriding plate. Unfortunately the petrological data for the overriding plate in Sulu UHP terrane is limited (Figure 1b) which does not allow comparison of the actual amount of up bending with our numerical modeling results.

[43] From the above comparison, our numerical model results show good agreement with the Sulu UHP terrane in terms of (1) spatial distribution of metamorphic units; (2) peak P-T conditions of the HP-UHP metamorphism; (3) temporal constraints for polyphase exhumation; and (4) mixed rock types.

6. Discussion

6.1. Cyclicity of "Thrust Faults" Formation and Exhumation of (U)HP Units

[44] One of the most important characteristics of numerical models presented in this study is the cyclic formation of the thrust faults (rheological weak zones), which is followed by exhumation processes (Figure 3). Similar detachment phenomenon is also documented in analog models of continental subduction [*Chemenda et al.*, 1995, 1996, 2000]. The behavior of the subducted continental crust depends on two competing effects: upward buoyancy and downward subduction drag [e.g., *Raimbourg et al.*, 2007; *Currie et al.*, 2007; *Warren et al.*, 2008b]. Subduction drag within the crust and mantle drives the subduction of buoyant crustal materials into larger depths (Figures 4a and 5a). At the same time the buoyancy forces and also the deviatoric stresses increase in the subduction channel (Figures 6a

Figure 11. Influences of the surface sedimentation and erosion rates on the first thrust fault formation (enlarged 500 × 210 km domains of the original 4000 × 670 km models). (a) Lower sedimentation rate (0.3 mm a^{-1}) and normal erosion rate (1.0 mm a^{-1}) (model zhda in Table 2). (b) Normal sedimentation rate (1.0 mm a^{-1}) and lower erosion rate (0.3 mm a^{-1}) (model zhdc in Table 2). (c) Reference model with normal sedimentation rate (1.0 mm a^{-1}) and normal erosion rate (1.0 mm a^{-1}) (model zhaa in Table 2). (d) Higher sedimentation rate (3.0 mm a^{-1}) and normal erosion rate (1.0 mm a^{-1}) (model zhdb in Table 2). (e) Normal sedimentation rate (1.0 mm a^{-1}) and higher erosion rate (3.0 mm a^{-1}) (model zhdd in Table 2). Colors of rock types are as in Figure 2. Time (Ma) of shortening is given. White numbered lines are isotherms in °C.

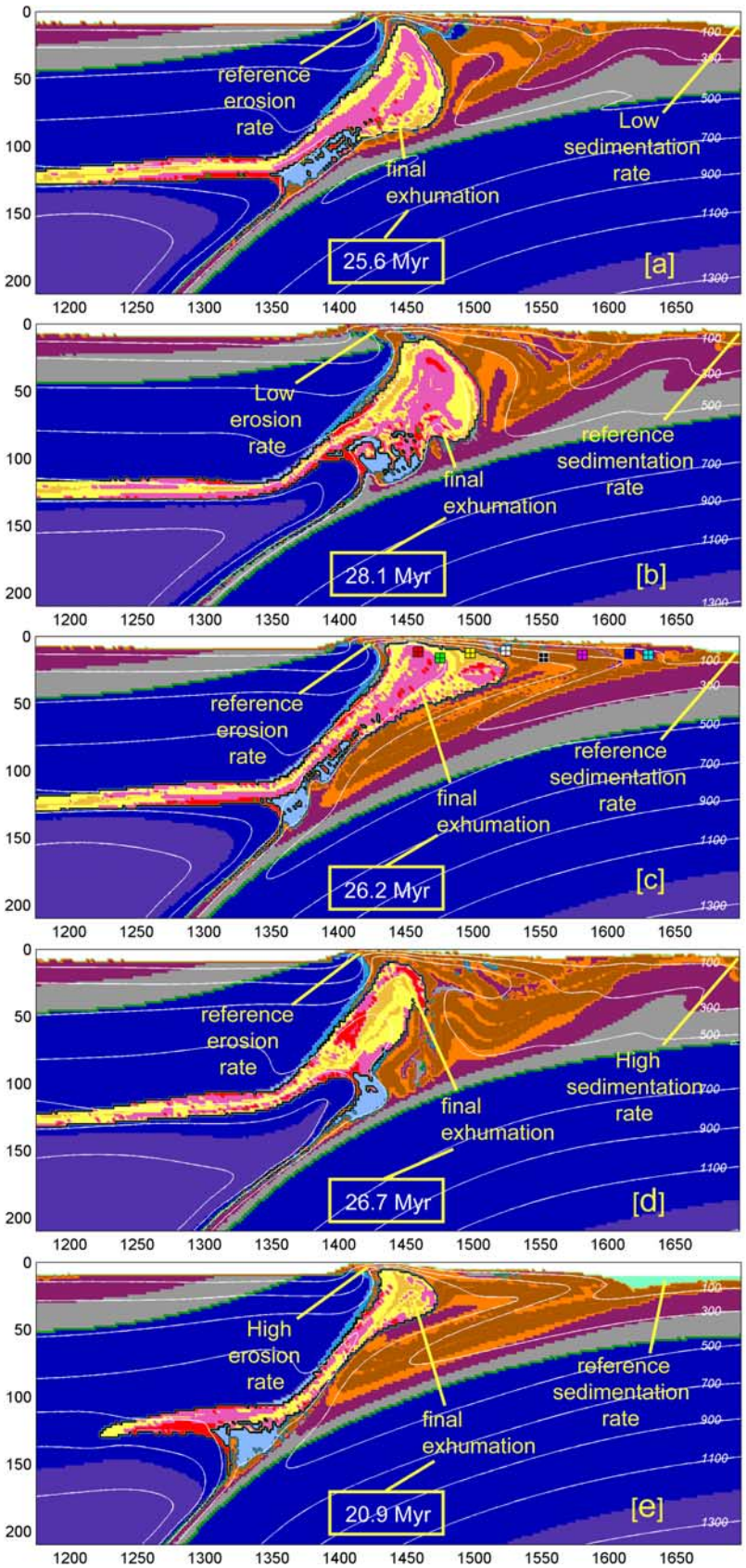
reference erosion rate
Low sedimentation rate
final exhumation
25.6 Myr
[a]
Low erosion rate
reference sedimentation rate
final exhumation
28.1 Myr
[b]
reference erosion rate
reference sedimentation rate
final exhumation
26.2 Myr
[c]
reference erosion rate
High sedimentation rate
final exhumation
26.7 Myr
[d]
High erosion rate
reference sedimentation rate
final exhumation
20.9 Myr
[e]
0
50
100
150
200
1200 1250 1300 1350 1400 1450 1500 1550 1600 1650

Figure 12

and 6b). When the materials are no longer strong enough to sustain the accumulated buoyancy and deviatoric stresses, the subducted continental crust will yield with forming the rheological weak zone (thrust fault) (Figures 4b, 4c, 5b, and 5c) followed by the detachment and exhumation of the buoyant crustal materials (Figures 4c, 4d, 5c, and 5d) and release of the accumulated buoyancy and deviatoric stresses (Figures 6c and 6d). After the first exhumation and deviatoric stresses release episode, crustal rocks continue subducting under the applied subduction drag. As soon as critical buoyancy and deviatoric stresses accumulate again, next episode of detachment and exhumation takes place (Figures 3d and 3e). Alternation of buoyancy/stress accumulation and release episodes makes subduction/exhumation processes during collision inherently cyclic which is reflected by variations in metamorphic ages of exhumed rock units (Figures 15b and 15d) gradually forming a poly metamorphic (U)HP terrane.

6.2. High-Temperature Conditions of the Exhumed UHP Terrane

[45] In the natural UHP terranes, the metamorphic temperature conditions (petrological thermal barometry) are commonly >700°C. However, in numerical models of UHP complexes, the temperature conditions are commonly by $\geq$100°C lower than those extracted from the natural data [e.g., *Stöckhert and Gerya*, 2005; *Yamato et al.*, 2007, 2008; *Warren et al.*, 2008a].

[46] It should be pointed out that initial temperature of rocks subducted to UHP conditions within subduction channel is relatively low (500–600°C, Figure 3c). If these rocks are exhumed shortly after reaching UHP depth (e.g., Figure 9) this lowered peak temperature is recorded by exhumed UHP rocks. In contrast, high-temperature (700–800°C) UHP conditions can be obtained when UHP rocks leave subduction channel, detach from the slab at asthenospheric depths and form horizontal sublithospheric plume. Formation of such compositionally buoyant plumes is well documented in both numerical [e.g., *Currie et al.*, 2007; *Gerya et al.*, 2008; *Warren et al.*, 2008a, 2008b] and analog [e.g., *Boutelier et al.*, 2004] models of subduction followed by collision. Our numerical models suggest that UHP rocks may remain in the sublithospheric plume for several million years being subjected to strong conductive heating from the surrounding hot mantle (Figure 3d). At the later stage upward extrusion of such hot partially molten rocks may exhume UHP-HT complexes toward the surface. Therefore, sublithospheric plume formation and extrusion processes may provide plausible explanation for occurrence of UHP-HT rocks in nature.

6.3. "Confined" and "Opened" Subduction Channel

[47] The main driving mechanisms of subduction are ridge "push" and slab "pull" [e.g., *Uyeda and Forsyth*, 1975], which are both present in our numerical models. In numerical experiments with various types of push and pull convergence conditions two types of subduction channel are formed: the "confined" channel and the "opened" channel. In most of our models (Figures 3a, 7a, 8a, 9a, and 10a), the prescribed constant convergence velocity produces the confined channel, indicating that the push forces dominate at the plate interface. In the models with changing convergence conditions (Figures 13 and 14), the opened channel forms gradually when the slab pull becomes dominating mechanism of subduction along with the decreasing convergence forces.

[48] Results obtained from the experiments with variable convergence conditions confirm that HP-UHP complexes can be formed in both confined and opened channel in the wide range of convergence scenarios. UHP rocks typically exhume after HP complexes within the rear portion of crustal wedge forming atop the subduction channel. Indeed, the tendencies of cyclic exhumation of HP-UHP rocks and deep subduction of continental crust associated with formation of a sublithospheric crustal plume are more pronounced in experiments where plate interface is strongly confined under an imposed lateral plate push.

7. Conclusion

[49] In agreement with poly phase origin of HP-UHP terranes our experiments predict existence of several consequent episodes of (U)HP rocks exhumation related to the inherently cyclic origin of continental crust subduction-detachment-exhumation processes. Periodicity of formation of rheologically weak zones (thrust faults) controlling HP-UHP rocks exhumation processes depends on the competing effects of downward directed subduction drag and upward directed crustal buoyancy forces. The buoyancy forces and related deviatoric stresses accumulate in the subduction channel due to subduction of low-density crustal rocks and are then reset back during rapid exhumation episodes. The reference model with intermediate parameters predicts three major phases of formation and exhumation of the HP-UHP metamorphic rocks in the continental subduction channel, which is applicable to the Sulu UHP terrane in eastern China.

Appendix A: Numerical Methodology

A1. Principal Equations

[50] The numerical modeling was employed using a finite difference numerical code (I2VIS) with marker-in-cell

Figure 12. Influences of the surface sedimentation and erosion rates on the final UHP rocks exhumation (enlarged 500 × 210 km domains of the original 4000 × 670 km models). (a) Lower sedimentation rate (0.3 mm a^{-1}) and normal erosion rate (1.0 mm a^{-1}) (model zhda in Table 2). (b) Normal sedimentation rate (1.0 mm a^{-1}) and lower erosion rate (0.3 mm a^{-1}) (model zhdc in Table 2). (c) Reference model with normal sedimentation rate (1.0 mm a^{-1}) and normal erosion rate (1.0 mm a^{-1}) (model zhaa in Table 2). (d) Higher sedimentation rate (3.0 mm a^{-1}) and normal erosion rate (1.0 mm a^{-1}) (model zhdb in Table 2). (e) Normal sedimentation rate (1.0 mm a^{-1}) and higher erosion rate (3.0 mm a^{-1}) (model zhdd in Table 2). Colors of rock types are as in Figure 2. Time (Ma) of shortening is given. White numbered lines are isotherms in °C.

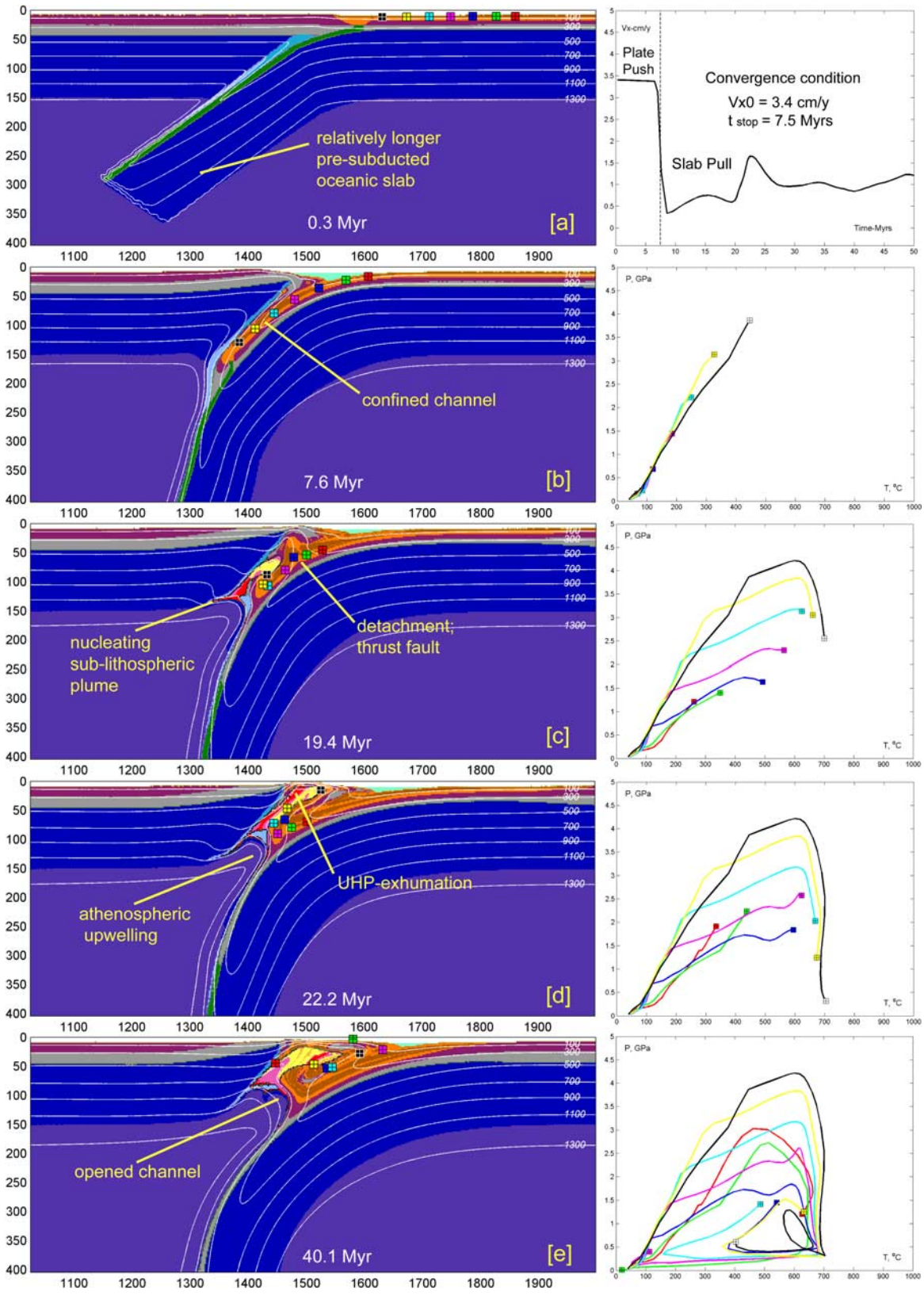

Figure 13. Evolution of the model with variable convergence condition (model zheb in Table 2). Enlarged 1000 × 410 km domain of the original 4000 × 670 km model is shown. Figure 13a shows the distribution of convergence velocity through time (the left section is ''plate push'' dominated and the right section is slab pull dominated). Colors of rock types are as in Figure 2. Time (Ma) of shortening is given. White numbered lines are isotherms in °C. P-T paths for positions of representative markers (rock units) which are indicated by small colored squares (with pluses).

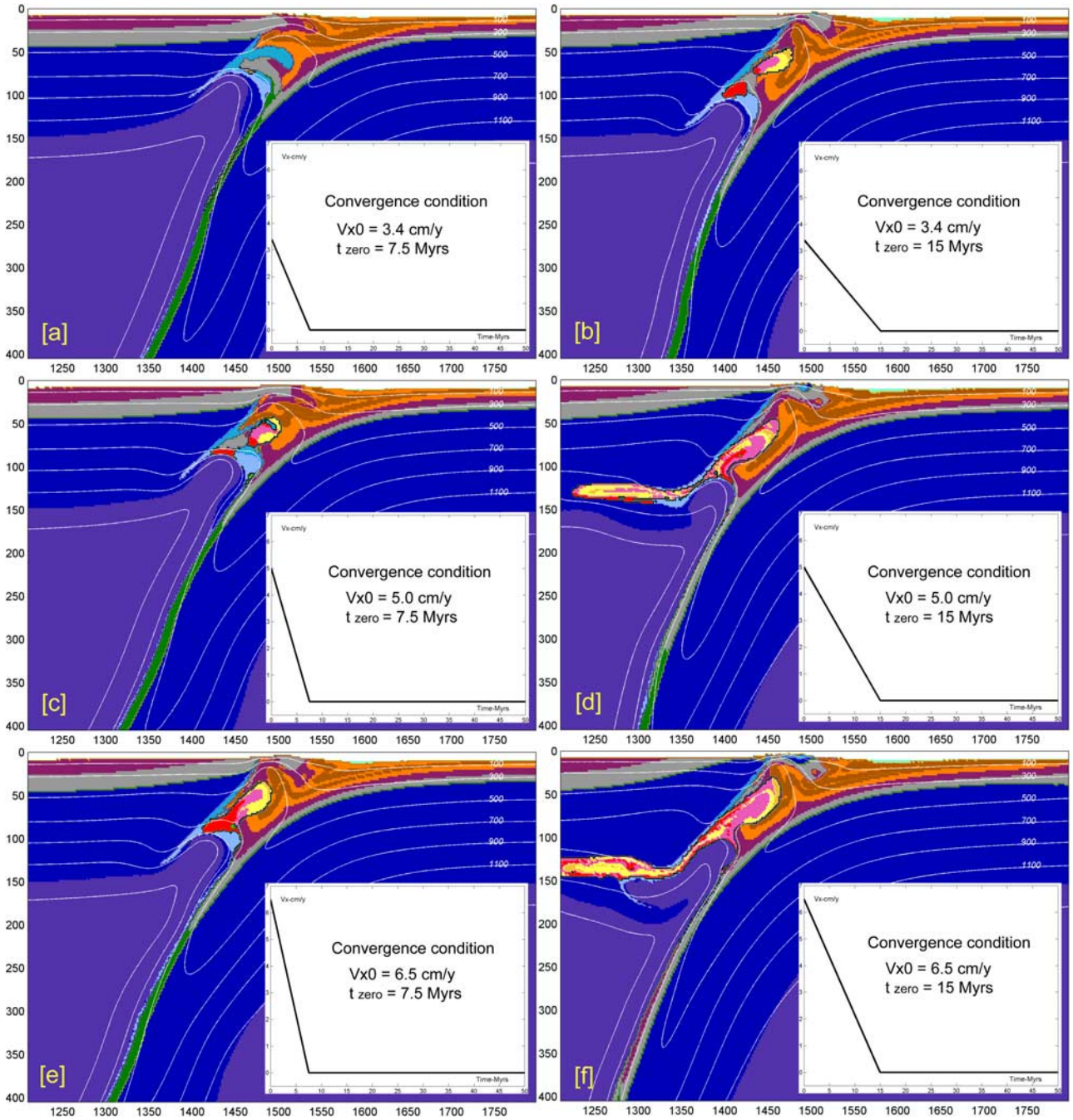

Figure 14. Comparison of models with linearly decreasing convergence velocity. Enlarged 600 × 410 km domain of the original 4000 × 670 km model is shown. Different prescribed velocities (v_{x0}) and timescales (t_{zero}) of the convergence condition are investigated (models zhed, zhee, zhef, zheg, zheh, zhei in Table 2). Colors of rock types are as in Figure 2. Time (Ma) of shortening is given in the figures. White numbered lines are isotherms in °C.

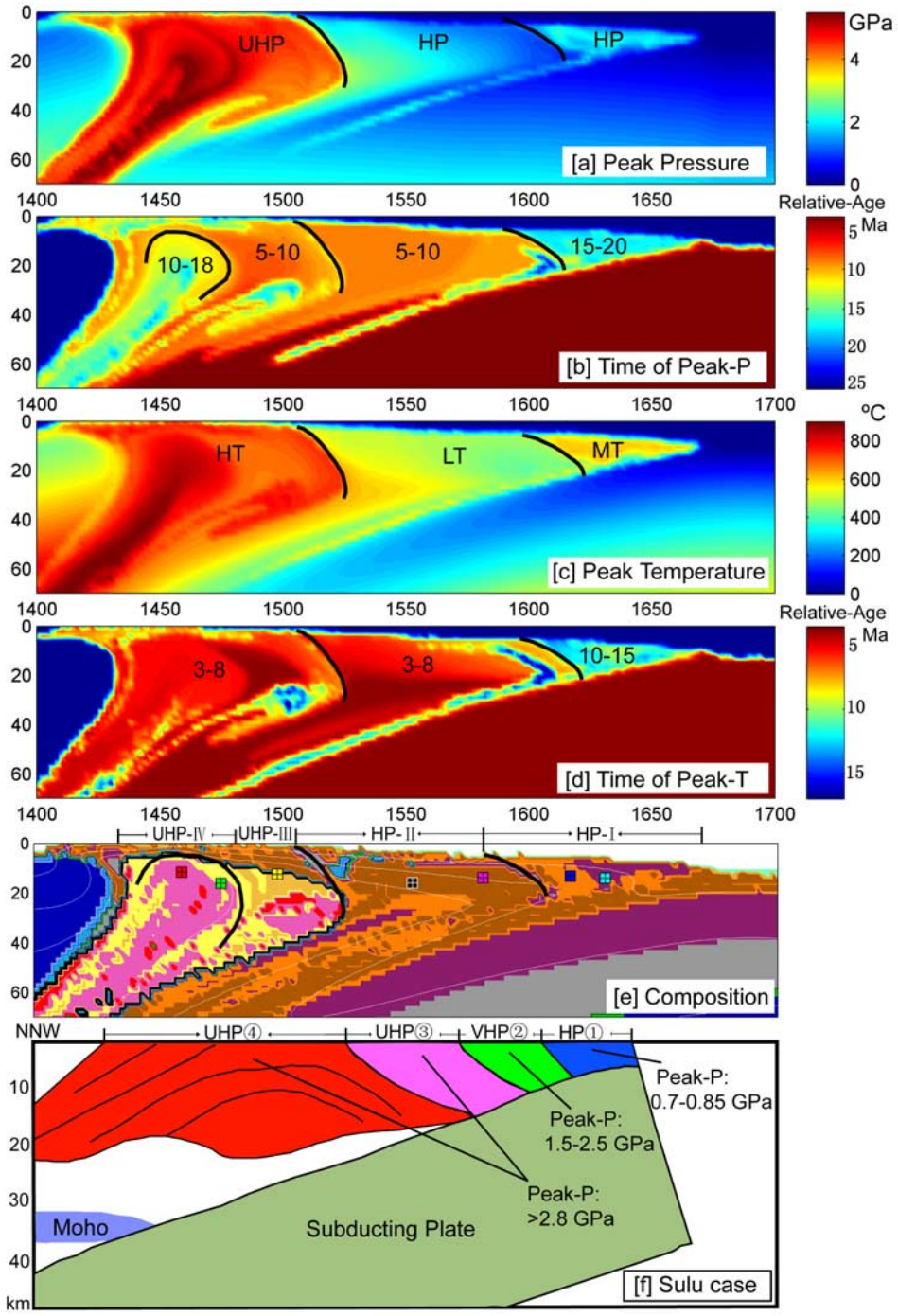

Figure 15. Metamorphic conditions of the HP-UHP slices (Figures 15a–15e) (enlarged 300 × 70 km domain of the final stage in the reference model, Figure 3f) and comparison with the Sulu UHP terrane (Figure 15f). (a) Peak pressure conditions in the domain. UHP, ultrahigh-pressure slices; HP, high-pressure slices. (b) Time of the peak pressure. Numbers show the "relative ages" (in Ma relative to the current stage) of the peak pressure conditions. (c) Peak temperature conditions in the domain. HT, high-temperature slices; LT, low-temperature slices; MT, middle-temperature slices. (d) Time of the peak temperature. Numbers show the relative ages (in Ma relative to the current stage) of the peak temperature conditions. (e) Material field with HP-UHP slices distribution (black lines): HP I, high-pressure slices in the first exhumation process; HP II, high-pressure slices in the second exhumation process; UHP III and IV, UHP slices in the final exhumation process. Colors of rock types are as in Figure 2. (f) Structure of Sulu HP-UHP terrane, revised from the integrated profile of *Yang* [2002]. HP 1, high-pressure slices; VHP 2, very high pressure slices; UHP 3, ultrahigh-pressure slices with protoliths mainly of sedimentary rocks; UHP 4, ultrahigh-pressure slices with protoliths mainly of granitic rocks. Peak pressure conditions are shown for each section.

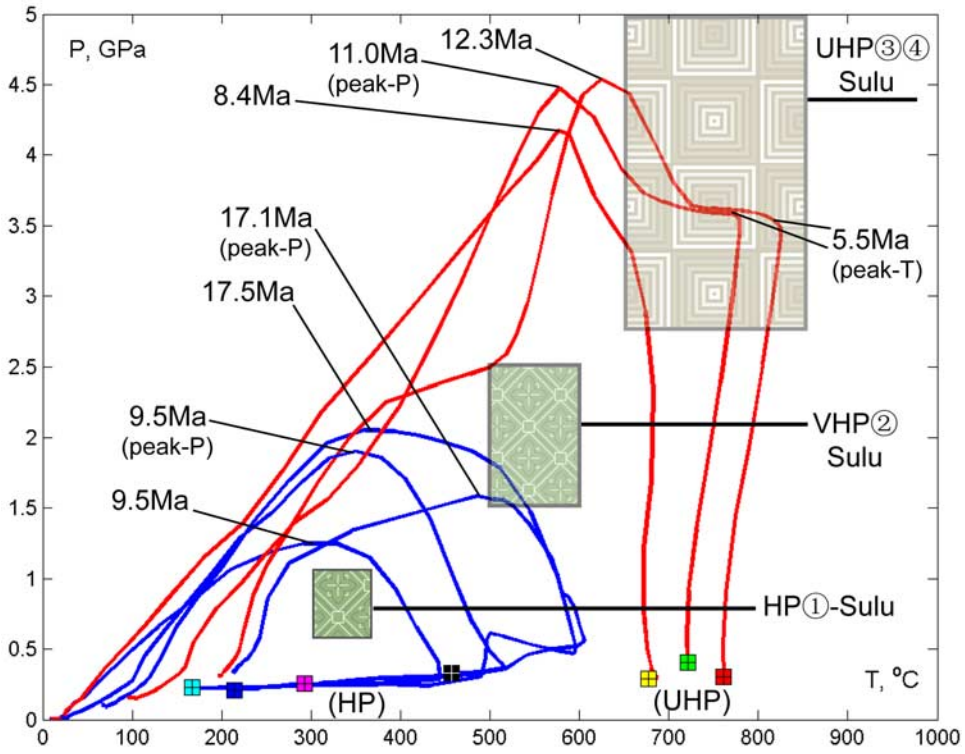

Figure 16. P-T-t paths of the numerical model and HP-UHP metamorphic conditions of the Sulu terrane. Red lines indicate P-T paths of the UHP slices in the numerical model (Figure 15e). Blue lines indicate P-T paths of the HP slices in the numerical model (Figure 15e). Corresponding markers are the same as in Figures 3f and 15e. Numbers on P-T paths (in Ma relative to the stage shown in Figures 15a–15e) show relative ages for peak pressure (P) and temperature (T) conditions. Filled rectangles indicate the P-T conditions of the Sulu HP-VHP-UHP slices.

technique [*Gerya and Yuen*, 2003a]. The momentum, continuity, and heat conservation equations for a 2-D creeping flow including thermal and chemical buoyant forces are solved within this code.

[51] 1. Two-dimensional stokes equations:

$$\frac{\partial \sigma_{xx}}{\partial x}+\frac{\partial \sigma_{xz}}{\partial z}=\frac{\partial P}{\partial x}$$
$$\frac{\partial \sigma_{zx}}{\partial x}+\frac{\partial \sigma_{zz}}{\partial z}=\frac{\partial P}{\partial z}-g\rho(C,M,P,T)$$

where the density ρ depends on composition (C), melt fraction (M), temperature (T) and pressure (P).

[52] 2. Conservation of mass is approximated by the incompressible continuity equation:

$$\frac{\partial v_x}{\partial x}+\frac{\partial v_z}{\partial z}=0$$

[53] 3. Heat conservation equations:

$$\rho C_p\left(\frac{DT}{Dt}\right)=-\frac{\partial q_x}{\partial x}-\frac{\partial q_z}{\partial z}+H_r+H_a+H_S+H_L$$
$$q_x=-k(T,P,C)\frac{\partial T}{\partial x},\ q_z=-k(T,P,C)\frac{\partial T}{\partial z}$$
$$H_a=T\alpha\frac{dP}{dt},\ H_S=\sigma_{xx}\varepsilon_{xx}+\sigma_{zz}\varepsilon_{zz}+2\sigma_{xz}\varepsilon_{xz}$$

where the thermal conductivity k depends on the temperature (T), pressure (P) and composition (C).

A2. Rheological Model

[54] A viscoplastic rheology is assigned to the model by means of a Christmas tree-like criterion, where the rheological behavior depends on the minimum differential stress attained between the ductile and brittle fields [*Ranalli*, 1995].

[55] Ductile viscosity dependent on strain rate, pressure and temperature is defined in terms of deformation invariants [*Ranalli*, 1995] as

$$\eta_{\text{creep}}=(\varepsilon_{II})^{(1-n)/n}F(A_D)^{-1/n}\exp\left(\frac{E+PV}{nRT}\right)$$

where $\varepsilon_{II}=\sqrt{(0.5\varepsilon_{ij}\varepsilon_{ij})}$ is the second invariant of the strain rate tensor and F is a dimensionless coefficient depending on the type of experiments on which the flow law is based. For example,

For triaxial compression $F=\dfrac{2^{(1-n)/n}}{3^{(1+n)/2n}}$

For simple shear $F=2^{(1-2n)/n}$

For solid rocks ($\leq$10 vol % melt), the ductile rheology is combined with a brittle/plastic rheology to yield an effective

viscoplastic rheology. For this purpose the Mohr-Coulomb yield criterion [e.g., *Ranalli*, 1995] is implemented as follows:

$$\sigma_{\text{yield}} = (N_1 P_{\text{lith}} + N_2)(1 - \lambda)$$

$$\eta_{\text{creep}} \leq \left(\frac{\sigma_{\text{yield}}}{(4\varepsilon_{II})^{1/2}} \right)$$

where N_1 and N_2 are empirical constants [*Brace and Kohlstedt*, 1980]; λ is the pore fluid coefficient that controls the brittle strength of fluid-containing porous or fractured media. The effective viscosity of molten rocks (>10 vol % melt) was assigned to a low value of 10^{19} Pa s.

A3. Partial Melting

[56] The numerical code accounts for partial melting of the various lithologies by using experimentally obtained P-T dependent wet solidus and dry liquidus curves [*Gerya and Yuen*, 2003b]. As a first approximation, volumetric melt fraction M is assumed to increase linearly with temperature accordingly to the following relations [*Burg and Gerya*, 2005]:

$$M = 0, \qquad T \leq T_{\text{solidus}}$$

$$M = \frac{(T - T_{\text{solidus}})}{(T_{\text{liquidus}} - T_{\text{solidus}})}, \qquad T_{\text{solidus}} < T < T_{\text{liquidus}}$$

$$M = 1, \ when: T \geq T_{liquidus}$$

where T_{solidus} and T_{liquidus} are the wet solidus and dry liquidus temperature of the given lithology, respectively (Table 1).

[57] Consequently, the effective density, ρ_{eff}, of partially molten rocks varies with the amount of melt fraction and P-T conditions according to the relations

$$\rho_{\text{eff}} = \rho_{\text{solid}} - M(\rho_{\text{solid}} - \rho_{\text{molten}})$$

where ρ_{solid} and ρ_{molten} are the densities of the solid and molten rock, respectively, which vary with pressure and temperature according to the relation

$$\rho_{P,T} = \rho_0[1 - \alpha(T - T_0)][1 + \beta(P - P_0)]$$

where ρ_0 is the standard density at $P_0 = 0.1$ MPa and $T_0 = 298$ K.

[58] The effects of latent heat H_L [e.g., *Stüwe*, 1995] are accounted for by an increased effective heat capacity (Cp_{eff}) and thermal expansion (α_{eff}) of the partially molten rocks ($0 < M < 1$), calculated as

$$Cp_{\text{eff}} = Cp + Q_L \left(\frac{\partial M}{\partial T} \right)_P$$

$$\alpha_{\text{eff}} = \alpha + \rho \frac{Q_L}{T} \left(\frac{\partial M}{\partial P} \right)_T$$

where Cp and α are the heat capacity and the thermal expansion of the solid crust, respectively, and Q_L is the latent heat of melting of the crust.

A4. Topography

[59] The spontaneous deformation of the upper surface of the lithosphere, i.e., topography, is calculated dynamically as an internal free surface by using a low viscosity (10^{18} Pa s), initially 8 km thick layer (thickness of this layer changes dynamically during experiments) above the upper crust (Figure 2). The composition is either "air" (1 kg m^{-3}, above z = 8.5 km water level) or "water" (1000 kg m^{-3}, below z = 8.5 km water level). The interface between this weak layer and the underlying crust is treated as an internal erosion/sedimentation surface which evolves according to the Eulerian transport equation solved in Eulerian coordinates at each time step [*Gerya and Yuen*, 2003b]:

$$\frac{\partial z_{es}}{\partial t} = v_z - v_x \frac{\partial z_{es}}{\partial x} - v_s + v_e$$

where z_{es} is the vertical position of the surface as a function of the horizontal distance; v_s and v_e are the sedimentation and erosion rates, respectively, which correspond to the relation

$$v_s = 0 \text{ mm a}^{-1}, \ v_e = v_{e0}, \text{ when } z_{es} < 7 \text{ km}$$

$$v_s = v_{s0} \text{ mm a}^{-1}, \ v_e = 0, \text{when } z_{es} > 7 \text{ km}$$

where v_{e0} and v_{s0} are the imposed constant large-scale erosion and sedimentation rates, respectively.

[60] **Acknowledgments.** We acknowledge the fund from China Scholarship Council (CSC) and the support from the 973 Project of Chinese Ministry of Science and Technology (2003CB716504) to Z.H.L. This work was also supported by ETH research grants TH-12/04-1, TH-12/05-3, SNF research grant 200021-113672/1 to T.V.G. Qin Wang and Zhiqin Xu are thanked for fruitful discussions. Thorough and constructive reviews by J. Wakabayashi, L. Jolivet, and an anonymous reviewer are much appreciated.

References

Agard, P., L. Jolivet, B. Vrielynck, E. Burov, and P. Monié (2007), Plate acceleration: The obduction trigger?, *Earth Planet. Sci. Lett.*, *258*, 428–441, doi:10.1016/j.epsl.2007.04.002.

Beaumont, C., R. A. Jamieson, M. H. Nguyen, and B. Lee (2001), Himalayan tectonics explained by extrusion of a low-viscosity crustal channel coupled to focused surface denudation, *Nature*, *414*, 738–742, doi:10.1038/414738a.

Beaumont, C., M. Nguyen, R. A. Jamieson, and S. Ellis (2006), Crustal flow modes in large hot orogens, in *Channel Flows, Ductile Extrusion and Exhumation in Continental Collision Zones*, edited by R. D. Law, M. P. Searle, and L. Godin, *Geol. Soc. Spec. Publ.*, *268*, 91–145, doi:10.1144/GSL.SP.2006.268.01.05.

Bittner, D., and H. Schmeling (1995), Numerical modeling of melting processes and induced diapirism in the lower crust, *Geophys. J. Int.*, *123*, 59–70, doi:10.1111/j.1365-246X.1995.tb06661.x.

Boutelier, D., A. I. Chemenda, and C. Jorand (2004), Continental subduction and exhumation of high-pressure rocks: Insights from thermo-mechanical laboratory modeling, *Earth Planet. Sci. Lett.*, *222*, 209–216, doi:10.1016/j.epsl.2004.02.013.

Brace, W. F., and D. T. Kohlstedt (1980), Limits on lithospheric stress imposed by laboratory experiments, *J. Geophys. Res.*, *85*(B11), 6248–6252, doi:10.1029/JB085iB11p06248.

Brown, M. (2006), Duality of thermal regimes is the distinctive characteristic of plate tectonics since the Neoarchean, *Geology*, *34*(11), 961–964, doi:10.1130/G22853A.1.

Brown, M. (2007), Metamorphic conditions in orogenic belts: A record of secular change, *Int. Geol. Rev.*, *49*, 193–234, doi:10.2747/0020-6814.49.3.193.

Burg, J.-P., and T. V. Gerya (2005), The role of viscous heating in Barrovian metamorphism of collisional orogens: Thermomechanical models and application to the Lepontine Dome in the central Alps, *J. Metamorph. Geol.*, *23*, 75–95, doi:10.1111/j.1525-1314.2005.00563.x.

Burov, E., L. Jolivet, L. Le Pourhiet, and A. Poliakov (2001), A thermomechanical model of exhumation of high pressure (HP) and ultra-high pressure (UHP) metamorphic rocks in Alpine-type collision belts, *Tectonophysics*, *342*, 113–136, doi:10.1016/S0040-1951(01)00158-5.

Carswell, D. A., S. J. Cuthbert, and E. J. Krogh Ravna (1999), Ultrahigh-pressure metamorphism in the western Gneiss Region of the Norwegian Caledonides, *Int. Geol. Rev.*, *41*, 955–966, doi:10.1080/00206819909465182.

Chemenda, A. I., M. Mattauer, J. Malavieille, and A. Bokun (1995), A mechanism for syn-collisional rock exhumation and associated normal faulting: Results from physical modeling, *Earth Planet. Sci. Lett.*, *132*, 225–232, doi:10.1016/0012-821X(95)00042-B.

Chemenda, A. I., M. Mattauer, and A. Bokun (1996), Continental subduction and a mechanism for exhumation of high-pressure metamorphic rocks: New modelling and field data from Oman, *Earth Planet. Sci. Lett.*, *143*, 173–182, doi:10.1016/0012-821X(96)00123-9.

Chemenda, A. I., J.-P. Burg, and M. Mattauer (2000), Evolutionary model of the Himalaya-Tibet system: Geopoem: Based on new modelling, geological and geophysical data, *Earth Planet. Sci. Lett.*, *174*, 397–409, doi:10.1016/S0012-821X(99)00277-0.

Chopin, C. (2003), Ultrahigh-pressure metamorphism: Tracing continental crust into mantle, *Earth Planet. Sci. Lett.*, *212*, 1–14, doi:10.1016/S0012-821X(03)00261-9.

Clauser, C., and E. Huenges (1995), Thermal conductivity of rocks and minerals, in *Rock Physics and Phase Relations*, *AGU Ref. Shelf*, vol. 3, edited by T. J. Ahrens, pp. 105–126, AGU, Washington, D. C.

Cong, B. L., and Q. C. Wang (1999), The Dabie-Sulu UHP rocks slice: Review and prospect, *Chin. Sci. Bull.*, *44*, 1074–1085, doi:10.1007/BF02886130.

Currie, C. A., C. Beaumont, and R. S. Huismans (2007), The fate of subducted sediments: A case for backarc intrusion and underplating, *Geology*, *35*(12), 1111–1114, doi:10.1130/G24098A.1.

Ellis, S., C. Beaumont, and O. A. Pffifner (1999), Geodynamic models of crustal-scale episodic tectonic accretion and underplating in subduction zones, *J. Geophys. Res.*, *104*(B7), 15,169–15,190, doi:10.1029/1999JB900071.

Ernst, W. G., and J. G. Liou (1995), Contrasting plate-tectonic styles of the Qinling-Dabie-Sulu and Franciscan metamorphic belts, *Geology*, *23*(4), 353–356, doi:10.1130/0091-7613(1995)023<0353:CPTSOT>2.3.CO;2.

Faccenda, M., T. V. Gerya, and S. Chakraborty (2008), Styles of post-subduction collisional orogeny: Influence of convergence velocity, crustal rheology and radiogenic heat production, *Lithos*, *103*, 257–287, doi:10.1016/j.lithos.2007.09.009.

Faure, M., W. Lin, U. Scharer, L. Shu, Y. Sun, and N. Arnaud (2003), Continental subduction and exhumation of UHP rocks: Structural and geochronological insights from the Dabieshan (east China), *Lithos*, *70*, 213–241, doi:10.1016/S0024-4937(03)00100-2.

Frey, M., J. Desmons, and F. Neubauer (1999), The new metamorphic map of the Alps, *Schweiz. Mineral. Petrogr. Mitt.*, *79*(1), spec. vol., 230 pp.

Gerya, T. V., and B. Stöckhert (2006), Two-dimensional numerical modeling of tectonic and metamorphic histories at active continental margins, *Int. J. Earth Sci.*, *95*, 250–274, doi:10.1007/s00531-005-0035-9.

Gerya, T. V., and D. A. Yuen (2003a), Characteristics-based marker-in-cell method with conservative finite-differences schemes for modeling geological flows with strongly variable transport properties, *Phys. Earth Planet. Inter.*, *140*, 293–318, doi:10.1016/j.pepi.2003.09.006.

Gerya, T. V., and D. A. Yuen (2003b), Rayleigh-Taylor instabilities from hydration and melting propel cold plumes at subduction zones, *Earth Planet. Sci. Lett.*, *212*, 47–62, doi:10.1016/S0012-821X(03)00265-6.

Gerya, T. V., B. Stöckhert, and A. L. Perchuk (2002), Exhumation of high-pressure metamorphic rocks in a subduction channel: A numerical simulation, *Tectonics*, *21*(6), 1056, doi:10.1029/2002TC001406.

Gerya, T. V., L. L. Perchuk, and J.-P. Burg (2008), Transient hot channels: Perpetrating and regurgitating ultrahigh-pressure, high-temperature crust-mantle associations in collision belts, *Lithos*, *103*, 236–256, doi:10.1016/j.lithos.2007.09.017.

Hacker, B. R., L. Ratschbacher, L. Webb, M. O. McWilliams, T. Ireland, A. Calvert, S. Dong, H.-R. Wenk, and D. Chateigner (2000), Exhumation of ultrahigh-pressure continental crust in east central China: Late Triassic–Early Jurassic tectonic unroofing, *J. Geophys. Res.*, *105*(B6), 13,339–13,364, doi:10.1029/2000JB900039.

Kaneko, Y., et al. (2000), Geology of the Kokchetav UHP-HP metamorphic belt, northern Kazakhstan, *Isl. Arc*, *9*, 264–283, doi:10.1046/j.1440-1738.2000.00278.x.

Labrosse, S., and C. Jaupart (2007), Thermal evolution of the Earth: Secular changes and fluctuations of plate characteristics, *Earth Planet. Sci. Lett.*, *260*, 465–481, doi:10.1016/j.epsl.2007.05.046.

Liou, J. G., Q. Wang, R. Zhang, M. Zhai, and B. Cong (1995), Ultrahigh-P metamorphic rocks and their associated lithologies from the Dabie Mountains, central China: A field trip guide to the 3rd International Eclogite Field Symposium, *Chin. Sci. Bull.*, *40*, 1–41.

Liou, J. G., T. Tsujimori, R. Y. Zhang, I. Katayama, and S. Maruyama (2004), Global UHP metamorphism and continental subduction/collision: The Himalayan model, *Int. Geol. Rev.*, *46*, 1–27, doi:10.2747/0020-6814.46.1.1.

Liu, D., P. Jian, A. Kröner, and S. Xu (2006), Dating of prograde metamorphic events deciphered from episodic zircon growth in rocks of the Dabie-Sulu UHP complex, China, *Earth Planet. Sci. Lett.*, *250*, 650–666, doi:10.1016/j.epsl.2006.07.043.

Liu, F., Z. Xu, and H. Xue (2004), Tracing the protolith, UHP metamorphism, and exhumation ages of orthogneiss from the SW Sulu terrane (eastern China): SHRIMP U-Pb dating of mineral inclusion-bearing zircons, *Lithos*, *78*, 411–429, doi:10.1016/j.lithos.2004.08.001.

Liu, F. L., A. Gerdes, J. G. Liou, H. M. Xue, and F. H. Liang (2006), SHRIMP U-Pb zircon dating from Sulu-Dabie dolomitic marble, eastern China: Constraints on prograde, ultrahigh-pressure and retrograde metamorphic ages, *J. Metamorph. Geol.*, *24*, 569–589, doi:10.1111/j.1525-1314.2006.00655.x.

Pope, D., and C. Willett (1998), Thermal-mechanical model for crustal thickening in the central Andes driven by ablative subduction, *Geology*, *26*(6), 511–514, doi:10.1130/0091-7613(1998)026<0511:TMMFCT>2.3.CO;2.

Qiu, H. J., and Z. Q. Xu (2002), New mineral evidence of high pressure metamorphism of the Subei high-pressure slice-Aragonite inclusions in garnet from greenschist, *Geol. Bull. China*, *21*, 617–624.

Raimbourg, H., L. Jolivet, and Y. Leroy (2007), Consequences of progressive eclogitization on crustal exhumation, a mechanical study, *Geophys. J. Int.*, *168*, 379–401, doi:10.1111/j.1365-246X.2006.03130.x.

Ranalli, G. (1995), *Rheology of the Earth: Deformation and Flow Processes in Geophysics and Geodynamics*, 2nd ed., Chapman and Hall, Boston, Mass.

Schmidt, M. W., and S. Poli (1998), Experimentally based water budgets for dehydrating slabs and consequences for arc magma generation, *Earth Planet. Sci. Lett.*, *163*, 361–379, doi:10.1016/S0012-821X(98)00142-3.

Stöckhert, B., and T. V. Gerya (2005), Pre-collisional high pressure metamorphism and nappe tectonics at active continental margins: A numerical simulation, *Terra Nova*, *17*, 102–110, doi:10.1111/j.1365-3121.2004.00589.x.

Stüwe, K. (1995), Thermal buffering effects at the solidus, Implications for the equilibration of partially melted metamorphic rocks, *Tectonophysics*, *248*, 39–51, doi:10.1016/0040-1951(94)00282-E.

Tao, W., and R. O'Connell (1992), Ablative subduction: A two-sided alternative to the conventional subduction model, *J. Geophys. Res.*, *97*(B6), 8877–8904, doi:10.1029/91JB02422.

Toussaint, G., E. Burov, and J.-P. Avouac (2004a), Tectonic evolution of a continental collision zone: A thermomechanical numerical model, *Tectonics*, *23*, TC6003, doi:10.1029/2003TC001604.

Toussaint, G., E. Burov, and L. Jolivet (2004b), Continental plate collision: Unstable vs. stable slab dynamics, *Geology*, *32*(1), 33–36, doi:10.1130/G19883.1.

Turcotte, D. L., and G. Schubert (1982), *Geodynamics: Application of Continuum Physics to Geological Problems*, 450 pp., John Wiley, New York.

Turcotte, D. L., and G. Schubert (2002), *Geodynamics*, 2nd ed., Cambridge Univ. Press, Cambridge, U. K.

Uyeda, S., and D. Forsyth (1975), On the relative importance of the driving forces of plate motion, *Geophys. J. R. Astron. Soc.*, *43*, 163–200.

Wakabayashi, J. (2004), Tectonic mechanisms associated with P-T paths of regional metamorphism: Alternatives to single-cycle thrusting and heating, *Tectonophysics*, *392*, 193–218, doi:10.1016/j.tecto.2004.04.012.

Wang, X., R. Zhang, and J. G. Liou (1995), UHPM terrane in east central China, in *Ultrahigh-Pressure Metamorphism*, edited by R. G. Coleman and X. Wang, pp. 356–390, Cambridge Univ. Press, Cambridge, U. K.

Warren, C. J., C. Beaumont, and R. A. Jamieson (2008a), Modelling tectonic styles and ultra-high pressure (UHP) rock exhumation during the transition from oceanic subduction to continental collision, *Earth Planet. Sci. Lett.*, *267*, 129–145, doi:10.1016/j.epsl.2007.11.025.

Warren, C. J., C. Beaumont, and R. A. Jamieson (2008b), Formation and exhumation of ultra-high-pressure rocks during continental collision: Role of detachment in the subduction channel, *Geochem. Geophys. Geosyst.*, *9*, Q04019, doi:10.1029/2007GC001839.

Xu, Z. Q., L. Zeng, F. Liu, J. Yang, Z. Zhang, M. McWilliams, and J. G. Liou (2006a), Polyphase subduction and exhumation of the Sulu high-pressure–ultrahigh-pressure metamorphic terrane, in *Ultrahigh-Pressure Metamorphism: Deep Continental Subduction*, edited by B. R. Hacker, W. C. McClelland, and J. G. Liou, *Spec. Pap. Geol. Soc. Am.*, *403*, 93–113.

Xu, Z. Q., X. Qi, J. Yang, L. Zeng, F. Liu, F. Liang, Z. Tang, and Z. Cai (2006b), Deep subduction erosion model for continental-continental col-

lision of the Sulu HP-UHP metamorphic terrain (in Chinese with English abstract), *Earth Sci. J. China Univ. Geosci.*, *31*, 4.

Yamato, P., P. Agard, E. Burov, L. Le Pourhiet, L. Jolivet, and C. Tiberi (2007), Burial and exhumation in a subduction wedge: Mutual constraints from thermomechanical modeling and natural P-T-t data (Schistes Lustre's, western Alps), *J. Geophys. Res.*, *112*, B07410, doi:10.1029/2006JB004441.

Yamato, P., E. Burov, P. Agard, L. Le Pourhiet, and L. Jolivet (2008), HP-UHP exhumation during slow continental subduction: Self-consistent thermodynamically and thermomechanically coupled model with application to the Western Alps, *Earth Planet. Sci. Lett.*, *271*, 63–74, doi:10.1016/j.epsl.2008.03.049.

Yang, W. (2002), Geophysical profiling across the Sulu ultra-high-pressure metamorphic belt, eastern China, *Tectonophysics*, *354*, 277–288, doi:10.1016/S0040-1951(02)00386-4.

Zhang, J., and R. Shi (2003), Deep tectonothermal mechanism for the tectonic extension of the eastern Asian continental margin, *Geotect. Metallogr.*, *27*, 156–164.

Zhang, R. Y., J. G. Liou, and J. F. Shuand (2002), Hydroxyl-rich topaz in high-pressure and ultrahigh-pressure kyanite quartzites, with retrograde woodhouseite, from the Sulu terrane, eastern China, *Am. Mineral.*, *87*, 445–453.

Zhang, R. Y., J. G. Liou, Y. F. Zheng, and B. Fu (2003), Transition of UHP eclogites to gneissic rocks of low-amphibolite facies during exhumation: Evidence from the Dabie terrane, central China, *Lithos*, *70*, 269–291, doi:10.1016/S0024-4937(03)00102-6.

Zhang, Z., Z. Xu, and H. Xu (2000), Petrology of ultrahigh-pressure eclogite from ZK703 drillhole in the Donghai, eastern China, *Lithos*, *52*, 35–50, doi:10.1016/S0024-4937(99)00083-3.

Zhang, Z., K. Shen, Y. Xiao, J. Hoefs, and J. G. Liou (2006), Mineral and fluid inclusions in zircon of UHP metamorphic rocks from the CCSD-main drill hole: A record of metamorphism and fluid activity, *Lithos*, *92*, 378–398, doi:10.1016/j.lithos.2006.04.003.

Zheng, Y. F., B. Fu, B. Gong, and L. Li (2003), Stable isotope geochemistry of ultrahigh pressure metamorphic rocks from the Dabie-Sulu orogen in China: Implications for geodynamics and fluid regime, *Earth Sci. Rev.*, *62*, 105–161, doi:10.1016/S0012-8252(02)00133-2.

T. V. Gerya, Geophysical Fluid Dynamics, Institute of Geophysics, Department of Earth Sciences, ETH-Zurich, CH-8092 Zurich, Switzerland.

Z. Li, Department of Earth Sciences, Nanjing University, 210093 Nanjing, China. (lzhhai@gmail.com)